

Orbital misalignment of the super-Earth π Men c with the spin of its star

Vedad Kunovac Hodžić¹★, Amaury H. M. J. Triaud¹, Heather M. Cegla^{2,3}†, William J. Chaplin^{1,4} and Guy R. Davies^{1,4}

¹*School of Physics and Astronomy, University of Birmingham, Edgbaston, Birmingham B15 2TT, UK*

²*Department of Physics, University of Warwick, Gibbet Hill Road, Coventry CV4 7AL, United Kingdom*

³*Observatoire de Genève, Université de Genève, Chemin des Maillettes 51, 1290 Sauverny, Switzerland*

⁴*Stellar Astrophysics Centre (SAC), Department of Physics and Astronomy, Aarhus University, Ny Munkegade 120, DK-8000 Aarhus C, Denmark*

Accepted XXX. Received YYY; in original form ZZZ

ABSTRACT

Planet-planet scattering events can leave an observable trace of a planet’s migration history in the form of orbital misalignment with respect to the stellar spin axis, which is measurable from spectroscopic timeseries taken during transit. We present high-resolution spectroscopic transits observed with *ESPRESSO* of the close-in super-Earth π Men c. The system also contains an outer giant planet on a wide, eccentric orbit, recently found to be inclined with respect to the inner planetary orbit. These characteristics are reminiscent of past dynamical interactions. We successfully retrieve the planet-occulted light during transit, and find evidence that the orbit of π Men c is moderately misaligned with the stellar spin axis with $\lambda = -24^\circ 0 \pm 4^\circ 1$ ($\psi = 26^\circ 9^{+5.8}_{-4.7}$). This is consistent with the super-Earth π Men c having followed a high-eccentricity migration followed by tidal circularisation, and hints that super-Earths can form at large distances from their star. We also detect clear signatures of solar-like oscillations within our *ESPRESSO* radial velocity timeseries, where we reach a radial velocity precision of $\sim 20 \text{ cm s}^{-1}$. We model the oscillations using Gaussian processes and retrieve a frequency of maximum oscillation, $\nu_{\text{max}} = 2771^{+65}_{-60} \mu\text{Hz}$. These oscillations makes it challenging to detect the Rossiter-McLaughlin effect using traditional methods. We are, however, successful using the *reloaded* Rossiter-McLaughlin approach. Finally, in an Appendix we also present physical parameters and ephemerides for π Men c from a Gaussian process transit analysis of the full *TESS* Cycle 1 data.

Key words: binaries: eclipsing – planetary systems – asteroseismology – techniques: radial velocity – techniques: spectroscopic

1 INTRODUCTION

Perhaps one of the most surprising results from two decades of exoplanet research is that planet sizes between that of Earth and Neptune ($1.5 R_\oplus$ to $2 R_\oplus$) are the most likely outcome of planet formation (e.g. Borucki et al. 2010; Batalha et al. 2013), even when such planets are completely absent from our own Solar System. Dubbed *super-Earths* (see Schlichting 2018 for a review), these planets orbit 50 % of Sun-like (FGK) stars (Howard et al. 2010; Mayor et al. 2011; Fressin et al. 2013), and rises to 75 % when including M dwarfs (Bonfils et al. 2013; Dressing & Charbonneau 2015; Gaidos et al. 2016; Hardegree-Ullman et al. 2019). The currently operating *TESS* survey (Ricker et al. 2015) is expected to find ~ 1000 additional super-Earths and mini-Neptunes in its 2-year nominal mission lifetime (Barclay et al. 2018; Huang et al. 2018a).

Yet for their abundance, there have been few observational constraints on their formation and dynamical evolution. In general, super-Earth formation consists of core formation followed by gas accretion onto the assembled core (Pollack et al. 1996; Chabrier et al. 2014). In the context of *in-situ* formation, the inner protoplanetary disk does

not have enough solid material in close-in feeding zones, such that any embryo will reach an isolation (maximum) mass well below that of super-Earths (Armitage 2013). Core accretion until isolation mass followed by a giant impact phase is also unlikely to produce the observed super-Earth population (Hansen & Murray 2012; Schlichting 2014; Dawson et al. 2016), which points to another likely mechanism at work to explain the close in super-Earths. Several super-Earths have been detected in circumbinary configurations (e.g. Orosz et al. 2019; Kostov et al. 2020). Due to strong gravitational perturbations produced by the binary orbital motion onto protoplanetary discs, planet formation is thought to only be possible at several AU from the central binaries (e.g. Paardekooper et al. 2012; Pierens et al. 2020) implying that the detected systems had to migrate in (Martin 2018; Pierens et al. 2020).

Close-in planet formation may be aided by an influx of solids in the form of pebbles (Johansen & Lambrechts 2017; Lambrechts et al. 2019), planetesimals, or even fully formed cores from a mass reservoir at several AU, where the isolation mass is higher. In either scenario, *in-situ* formation or inwards gas disk migration (see Baruteau et al. 2014 for a review), planets would remain aligned with the stellar equator, even in the event of interactions in multi-planet systems (Bitsch et al. 2013).

This is not the case for high-eccentricity migration, which can

★ Contact: vxh710@bham.ac.uk

† CHEOPS Fellow, SNSF NCCR-Planets

deliver fully formed super-Earths (or even hot Jupiters) to close-in, *inclined* orbits from beyond the snowline. In this two-step process, an outer giant planet will scatter the super-Earth to a highly elliptical orbit. At each periastron passage, the super-Earth will pass very close to the star (a few hundredths of AU) and cause tidal dissipation in the planet, which acts to reduce the orbital energy and circularise the orbit to its present day location. The initial scattering event produces a broad distribution of orbital inclinations (Fabrycky & Tremaine 2007; Naoz et al. 2011; Chatterjee et al. 2008), unlike the aforementioned disk migration pathways that results in co-planar systems.

One of the most promising ways of distinguishing different migration pathways is through the Rossiter-McLaughlin effect (Rossiter 1924; McLaughlin 1924), which measures the projected spin-orbit angle between the orbital plane and stellar spin axis, λ . Rossiter-McLaughlin measurements have all but become routine observables for hot Jupiters, and a trend has emerged in which stars above the Kraft break ($T_{\text{eff}} \gtrsim 6200$ K) tend to host misaligned massive planets, while stars below (cold stars) tend to have co-planar planets (see Triaud 2018 for a review, and references therein). In general this can be explained by hot Jupiters being massive enough to realign the stellar spin axis from tidal coupling to the their thick convective envelopes, and spin-down due to magnetic breaking, while more massive stars have thinner – or non-existent – convective envelopes and remain fast rotators (Winn et al. 2010b; Dawson 2014). These considerations muddle our interpretation of the dynamical histories of exoplanets, and thus inferring the migration pathways and formation mechanisms of close-in massive planets from spin-orbit angle measurements therefore remains difficult. Smaller planets, however – such as super-Earths – are not massive enough to realign the star within the tidal decay timescale or lifetime of the star (Dawson 2014), and will therefore keep their orbital inclinations, allowing us to robustly infer their migration pathways from their present-day orbital obliquities. However, Rossiter-McLaughlin observations have thus far largely eluded the super-Earths. The expected radial velocity semi-amplitudes are often at or below the m/s level, which is at the precision limit of our best spectrographs on the brightest stars, and where phenomena such as stellar oscillations and near-surface convection begin to dominate the signal. Nevertheless, successful Rossiter-McLaughlin campaigns have been carried out on small planets, such as the misaligned Neptune-mass exoplanets HAT-P-11 b (Winn et al. 2010a; Hirano et al. 2011), GJ 436 b (Bourrier et al. 2018), the somewhat contentious result on the super-Earth 55 Cnc e (Bourrier & Hébrard 2014; López-Morales et al. 2014), and most recently on the 22 Myr Neptune-sized planet AU Mic b (Addison et al. 2020; Hirano et al. 2020; Palle et al. 2020).

Here, we present a detection of the planetary shadow of a close-in super-Earth, known to host a giant planet companion on a wide, eccentric orbit. We find that the orbit is misaligned with the stellar spin-axis, pointing to an origin beyond the snowline and may show evidence of high-eccentricity migration following dynamical interaction with the outer companion in the system’s youth. We present spectroscopic transits obtained with the *ESPRESSO* spectrograph (Pepe et al. 2014), as one of the first science observations after completing its commissioning, and demonstrate its capabilities for providing observational constraints on planet formation of the most common population of exoplanets.

The paper is organised as follows: In Section 2 we present our analyses of the *ESPRESSO* data that includes *i*) modelling of the Rossiter-McLaughlin anomaly combined with a Gaussian process model for the asteroseismic activity, and *ii*) an independent analysis using the reloaded Rossiter-McLaughlin method. In addition, in Appendix A we include our transit analysis using the full *TESS* Cycle 1

Table 1. Summary of *ESPRESSO* and *TESS* data used in this work.

<i>ESPRESSO</i> (Section 2)						
ESO ID	Run	Night	N_{obs}	t_{exp} (s)	$\langle \text{SNR} \rangle$	$\langle \sigma_{\text{RV}} \rangle$ (cm s^{-1})
2012.C-5008(A)	A	2018-11-02	111	120	272	24
2012.C-5008(B)	B	2018-12-16	171	80	200	35
<i>TESS</i> (Appendix A)						
Sector	Date	N_{obs}	t_{exp} (s)	σ_{residual} (ppm)		
1	25 July – 22 August 2018	18 054	120	124		
4	18 October – 15 November 2018	15 768	120	114		
8	2 – 28 February 2019	13 395	120	133		
11	22 April – 21 May 2019	15 299	120	120		
12	21 May – 19 June 2019	19 071	120	137		
13	19 June – 18 July 2019	19 562	120	110		

data to inform our Rossiter-McLaughlin modelling. In Section 3 we present our updated transit parameters, and new asteroseismic parameters and obliquity measurements. We discuss our results in the context of planet formation in Section 4, and conclude in Section 5. In Appendix A we present our analysis on *TESS* photometric data to constrain the transit ephemerides and parameters for the Rossiter-McLaughlin analysis.

2 *ESPRESSO* DATA ANALYSIS

2.1 Observations and data reduction

Two transits of π Men c were observed on the nights of 2 November 2018 (run A) and 16 December 2018 (run B) using the *ESPRESSO* spectrograph (Pepe et al. 2014) mounted on the Very Large Telescope at ESO Paranal Observatory (DDT 2102.C-5008, PI: Hodžić). The transit in run A was observed concurrently with *TESS* Sector 4 observations. *ESPRESSO* observations were carried out under very good conditions (seeing $\sim 0.5''$) in the high-resolution mode using 1x1 binning. Integration times were fixed at 120 s and 80 s for run A and B, respectively, with 44 s dead-time per observation due to read-out, reaching median SNR per pixel of 272 and 200 at 550 nm for each run. The two runs cover respectively 5 h and 6 h uninterrupted sequences that cover the full transit duration and additional baselines of 2 h to 3 h before and after the transits. The observations are summarised in Table 1 (top).

The spectra were reduced with version 2.0 of the *ESPRESSO* data reduction pipeline¹, using a G2 binary mask to create cross-correlation functions (CCFs) that are fitted with Gaussian profiles. From the Gaussian fits we derive the depth (contrast), width (FWHM), and mean (radial velocity). The first sequence shows some variation in the derived contrast and SNR throughout the night which may be due to passing thin clouds. In Section 2.4.1 we describe a way of mitigating its impact on our result. The second sequence is stable with the contrast normally dispersed around the mean, but with a

¹ [ftp://ftp.eso.org/pub/dfs/pipelines/espreso/espdr-reflex-tutorial-1.0.0.pdf](http://ftp.eso.org/pub/dfs/pipelines/espreso/espdr-reflex-tutorial-1.0.0.pdf)

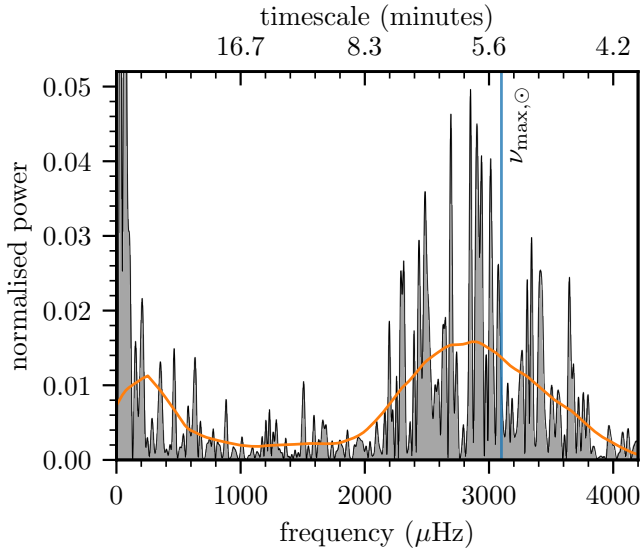


Figure 1. Lomb-Scargle periodogram of the combined *ESPRESSO* radial velocity data. The orange curve shows the heavily smoothed spectrum and reveals an estimate of $\nu_{\max} \approx 2900 \mu\text{Hz}$. In blue we denote the frequency of maximum oscillation for the Sun for comparison.

slope as the SNR increases throughout the night. The resulting median uncertainties on the integrated radial velocities are 24 cm s^{-1} and 35 cm s^{-1} for the first and second sequence, respectively.

The choice of exposure time for run B was informed by a preliminary analysis of run A, which showed two possible solutions for the frequency of maximum oscillation. We therefore opted for faster sampling rate in run B while still making sure to reach the required radial velocity precision for the Rossiter-McLaughlin effect.

2.2 Detection of solar-like oscillations in *ESPRESSO* data

Our initial approach to obtain the spin-orbit angle of π Men c is to fit the Rossiter-McLaughlin effect from the *ESPRESSO* radial velocity timeseries. The expected amplitude of the Rossiter-McLaughlin effect for this system (assuming $\lambda \sim 0^\circ$) is $\sim 50 \text{ cm s}^{-1}$. In this section, we shall see that the radial velocity timeseries is dominated by variability due to oscillations with amplitudes of a few m s^{-1} , which makes it challenging to extract the signal of the Rossiter-McLaughlin effect. Before attempting to detect the transiting planet, we first need to characterise the oscillation signal.

Fig. 1 shows the frequency power spectrum of the *ESPRESSO* radial velocity residuals. Here, we joined the two segments of data together, and then computed the spectrum using a Lomb-Scargle periodogram (Press & Rybicki 1989), sampled at a frequency resolution that corresponds to the inverse of the length of the combined dataset. The spectrum shows a clear excess of power due to solar-like oscillations (p -modes), centred around a frequency of maximum oscillations power of $\nu_{\max} \approx 2800 \mu\text{Hz}$. Note that the approach of joining together the two Doppler timeseries does not affect the detectability of the oscillations, because the damping times of the detectable modes are much shorter (of the order of a few days) than the gap between the two sets of data.

Owing to the very short duration of the combined dataset, it is not possible to resolve the individual overtones of the oscillation spectrum. The excess power due to the oscillations may as such be modelled to first order in these data as a Gaussian or Lorentzian in

frequency (here we choose the latter; see, e.g., Farr et al. 2018). Note the orange line in Fig. 1 shows the result of smoothing the spectrum with a double-boxcar filter of width $735 \mu\text{Hz}$.

We also searched the combined *TESS* residual light curve (after removing the transit and Gaussian process signal) for solar-like oscillations, but were unable to uncover evidence of detectable modes. However, as we shall see in the next section, the high S/N *ESPRESSO* data do show clearly detectable oscillations in Doppler velocity.

2.3 Gaussian process modelling of asteroseismic signal and Rossiter-McLaughlin effect

In this section we build on our analysis from Kunovac-Hodzic & Triaud (2019) to try to recover the “classical”, or velocimetric, Rossiter-McLaughlin effect. As is evident from Fig. 1, our data show clear signals from oscillations due to p -modes and possibly other lower frequency stellar activity. In recent years, Gaussian processes (GPs) have been shown to be robust models to describe correlated noise, stellar rotation, or other activity at various timescales (e.g. Haywood et al. 2014; Grunblatt et al. 2015; Gillen et al. 2017; Angus et al. 2018). Recently, there have also been examples of applying CARMA models (Farr et al. 2018) or Gaussian processes (Foreman-Mackey et al. 2017) to asteroseismic analyses in the time-domain. This allows for simultaneous transit or Keplerian modelling, whereas it has traditionally been done in frequency space. Following Foreman-Mackey et al. (2017), the oscillations may be modelled as a sum of stochastically driven damped simple harmonic oscillators (SHO), with power spectrum $S(\omega)$ given by

$$S(\omega) = \sqrt{\frac{2}{\pi}} \frac{S_0 \omega_0^4}{(\omega^2 - \omega_0^2)^2 + \omega_0^2 \omega^2 / Q^2}, \quad (1)$$

ω_0 is the peak angular frequency, S_0 is the maximum power, Q is the quality factor that describes the damping timescale. For large Q , Eq. 1 approaches a single-peaked Lorentzian function, and for modelling oscillations from different modes, Q would describe their damping timescale. From Section 2.2 we determined our dataset is too short to resolve individual overtones of the power spectrum, thus we only use a single SHO term (whose power spectrum is described by Eq. 1) to capture the overall shape of the p -mode power excess, and in this case Q will effectively describe the width of the power envelope. Similar assumptions have been made in e.g. Farr et al. (2018). The covariance function of Eq. 1 is a type of quasi-periodic function, given by

$$k(\tau) = S_0 \omega_0 Q \exp\left(-\frac{\omega_0 \tau}{2Q}\right) \cos(\eta \omega_0 \tau) + \frac{1}{2\eta Q} \sin(\eta \omega_0 \tau), \quad (2)$$

where τ is the lag between two measurements in time, and $\eta = \sqrt{|1 - 1/4Q^2|}$.

In addition to the oscillations, the data show an additional lower frequency variability component. The variability does not appear to be periodic, but has characteristics of correlated (red) noise which may originate from stellar surface convection or instrumental/environmental effects. In the case of run A, the background component may be dominated by changes in SNR due to varying observing conditions, see Fig. B1. Hereafter we refer to this as the “background” component, and let it encapsulate any variability that is not constrained by the oscillations model or the Rossiter-McLaughlin signal. A similar model to Eq. 1 can be used to describe the background term by fixing $Q = 1/\sqrt{2}$. In this case, the power spectral

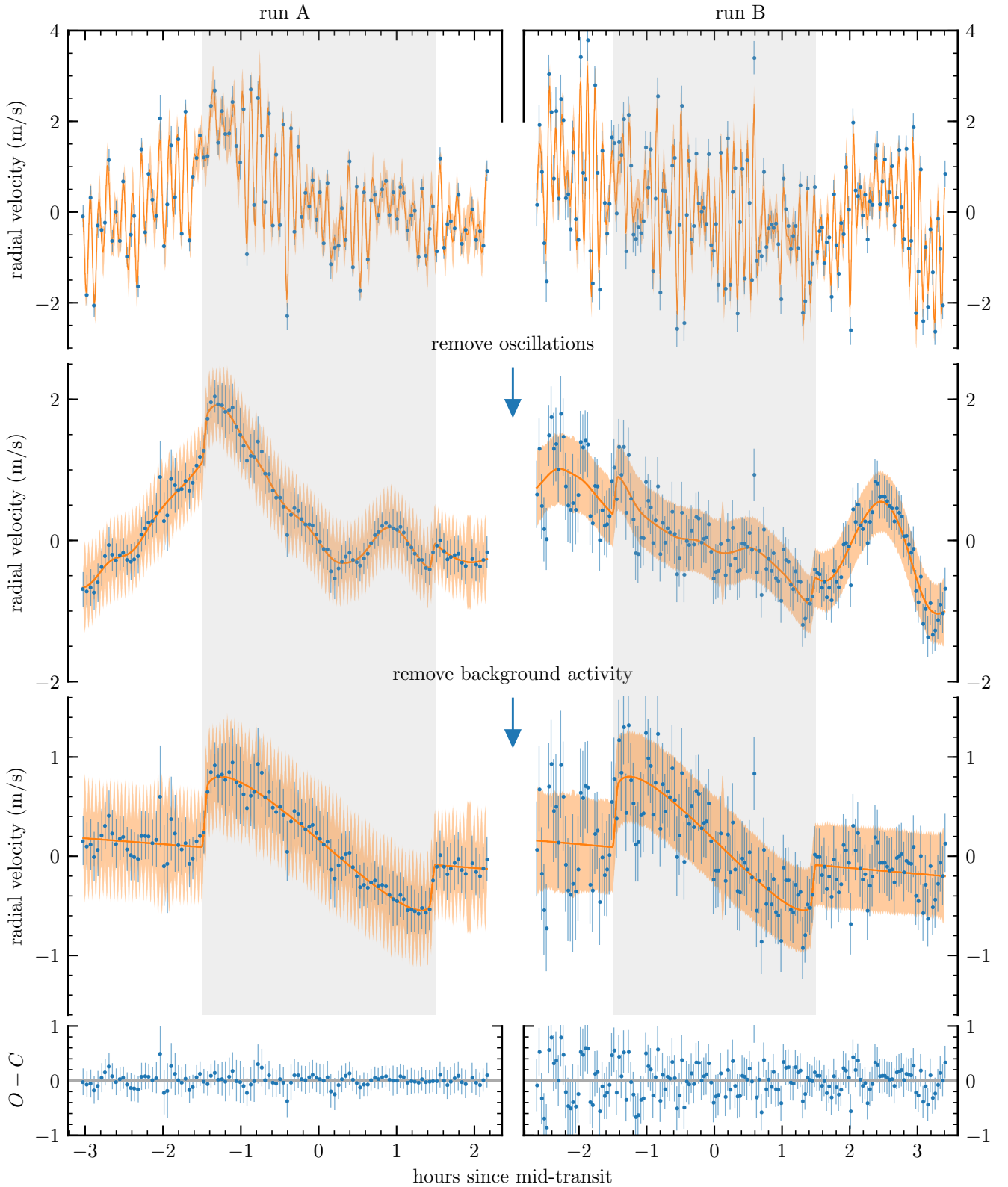


Figure 2. *Top:* ESPRESSO data from run A (*left*) and run B (*right*). The orange line is the best fit from our combined Rossiter-McLaughlin model and Gaussian process (GP) model (oscillations and “background” variability). The shaded area is the 68% (1σ) credible interval of the fit. *Upper middle:* The data after removing the contribution from oscillations in our GP model. *Lower middle:* The data after further removing the contribution from the longer-term variability in our GP model. *Bottom:* Residuals of the fit. The grey, shaded regions denote the transit duration.

Table 2. Priors on the Gaussian process hyperparameters for the radial velocity modelling.

Parameter	Prior
$\ln S_{\text{osc}}$ ($\text{km}^2 \text{s}^{-2}$)	$\mathcal{U}(-35, 15)$
$\ln Q_{\text{osc}}$	$\mathcal{U}(0, 4)$
ν_{max} (μHz)	$\mathcal{U}(2100, 4000)$
$\ln S_{\text{bkg}}$ ($\text{km}^2 \text{s}^{-2}$)	$\mathcal{U}(-35, -10)$
$\ln \omega_{\text{bkg}}$ (day^{-1})	$\mathcal{U}(3, 5.75)$
$\ln \sigma_A$ (km s^{-1})	$\mathcal{U}(-15, -4)$
$\ln \sigma_B$ (km s^{-1})	$\mathcal{U}(-15, -4)$

density given in Eq. 1 simplifies to

$$S(\omega) = \sqrt{\frac{2}{\pi}} \frac{S_0}{(\omega/\omega_0)^4 + 1}, \quad (3)$$

which describes a Harvey-like model commonly used to describe the background power due to surface convection (granulation) in asteroseismic and helioseismic analyses (Harvey 1985), but has also been used to model correlated signals in both radial velocity data and photometry (Foreman-Mackey et al. 2017). The covariance function for the background model simplifies to

$$k(\tau) = S_0 \omega_0 \exp\left(-\frac{\omega_0 \tau}{\sqrt{2}}\right) \cos\left(\frac{\omega_0 \tau}{\sqrt{2}} - \frac{\pi}{4}\right). \quad (4)$$

We use the *celerite* Gaussian processes software (Foreman-Mackey et al. 2017) to model the stellar signals together with a Rossiter-McLaughlin model. We use the simple harmonic oscillator (SHO) kernel within *celerite*, which is a type of quasi-periodic kernel whose power spectral density and covariance function are described by Eqs. 1 and 2. We fit for the frequency of maximum oscillation power, $\nu_{\text{max}} = \omega_{\text{max}}/2\pi$, logarithm of the amplitude $\ln S_{\text{osc}}$, and power-excess width, $\ln Q_{\text{osc}}$ to fit the high-frequency variations in our data, which was clearly favoured by the Bayesian Information Criterion (BIC). We include an additional SHO term with PSD given by Eq. 3 and covariance function by Eq. 4 for the low frequency background component, where Q is fixed to $1/\sqrt{2}$, and is also clearly favoured by the BIC. Here we fit for the logarithm of the amplitude $\ln S_{\text{bkg}}$, and angular frequency $\ln \omega_{\text{bkg}}$. We attempted to also include a second background term, but found no support for a second signal from a comparison of the BIC.

The oscillation timescale is only a few times that of our cadence, which can potentially introduce smearing of the oscillation signal. To account for this, we use integrated versions of the *celerite* kernels that we introduced above (Dan Foreman-Mackey, private comm.). However, we found that this effect did not make a noticeable difference on our result. Moreover, inspecting the data in Fig. 2, the noise properties of the two sequences appear qualitatively different. We therefore model the two *ESPRESSO* timeseries with individual Gaussian process kernels since their covariance properties are expected to differ, but share the hyperparameters between them. The priors on the hyperparameters are shown in Table 2.

Our orbital model is computed using *ellc*, where the Rossiter-McLaughlin effect is computed as the flux-weighted radial velocity, as included in the package. We vary the transit parameters with Gaussian priors based on the posterior distribution obtained from our *TESS* photometric analysis, outlined Appendix A, which are listed in Table 4. The radial velocity semi-amplitude is also varied with a Gaussian prior $K = 1.5 \pm 0.2 \text{ m s}^{-1}$, according to the most recent radial velocity orbit analysis in Damasso et al. (2020), which

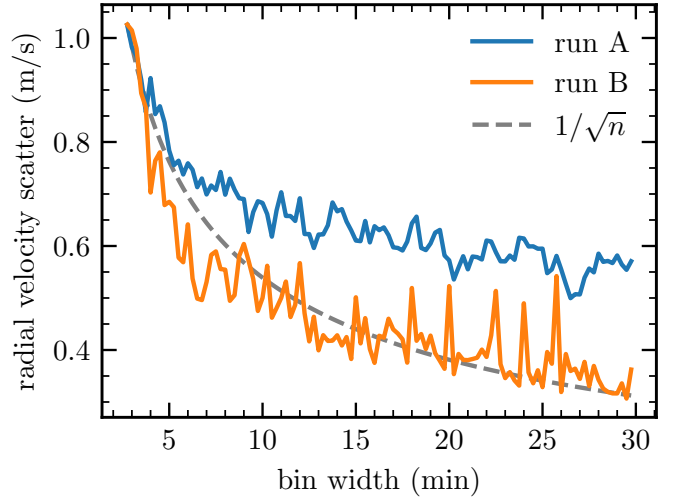


Figure 3. Radial velocity scatter as function of bin width for run A (blue) and run B (orange). The black dashed line denotes the expectation from white noise scaling.

is in agreement with Huang et al. (2018b) and Gandolfi et al. (2018). For the Rossiter-McLaughlin effect we fit for the projected rotation, $v_{\text{eq}} \sin i_{\star}$, of the star, and the spin-orbit angle, λ , and restrict their values to $v_{\text{eq}} \sin i_{\star} \sim \mathcal{U}(0, 20) \text{ km s}^{-1}$, $\lambda \sim \mathcal{U}(-180^{\circ}, 180^{\circ})$.

The free parameters in our joint Gaussian process and Rossiter-McLaughlin model are sampled using the *emcee* package (Foreman-Mackey et al. 2013). Given the relatively large number of parameters, we launch 400 “walkers” that we run for ~ 50 times the estimated autocorrelation length of the parameters. We discard the samples associated with a burn-in phase, which we determined visually, and then checked for convergence by verifying that all parameters reached $\hat{R} < 1.1$ (Gelman et al. 2003). The chains were further thinned by their estimated autocorrelation length before merging them, resulting in > 1000 effective samples per parameter.

As we shall see in Section 3, the detection of the Rossiter-McLaughlin effect is uncertain using the velocimetric method outlined in this section. Therefore, as a next step, we attempt to directly analyse the line profile distortion due to the planet in the next section.

2.4 Rossiter-McLaughlin reloaded

2.4.1 Retrieving the occulted light

A relatively recent method termed the reloaded Rossiter-McLaughlin method (Cegla et al. 2016; Bourrier et al. 2017, 2018; Ehrenreich et al. 2020; Kunovac Hodžić et al. 2020) uses the cross-correlation functions (CCF) to retrieve the light on the stellar disc that is occulted by the planet during transit, and has been shown to address some issues that may bias measurements of λ in “classical” Rossiter-McLaughlin analyses, such as the method presented in Section 2.3. In summary, the in-transit CCFs (CCF_{in}) are subtracted from a reference out-of-transit CCF (CCF_{out}) to retrieve the local stellar CCF behind the planet. We refer the reader to Cegla et al. (2016) for more details, and also similar, pioneering methods in Albrecht et al. (2007) and Collier Cameron et al. (2010). In the following we will use the abbreviation “DI” to refer to “disc-integrated” CCFs, to make clear the distinction from the “local” CCFs. Local CCF refers to the retrieved stellar light behind the planet, i.e. Doppler shadow.

The continuum levels of *ESPRESSO* CCFs are arbitrary due to

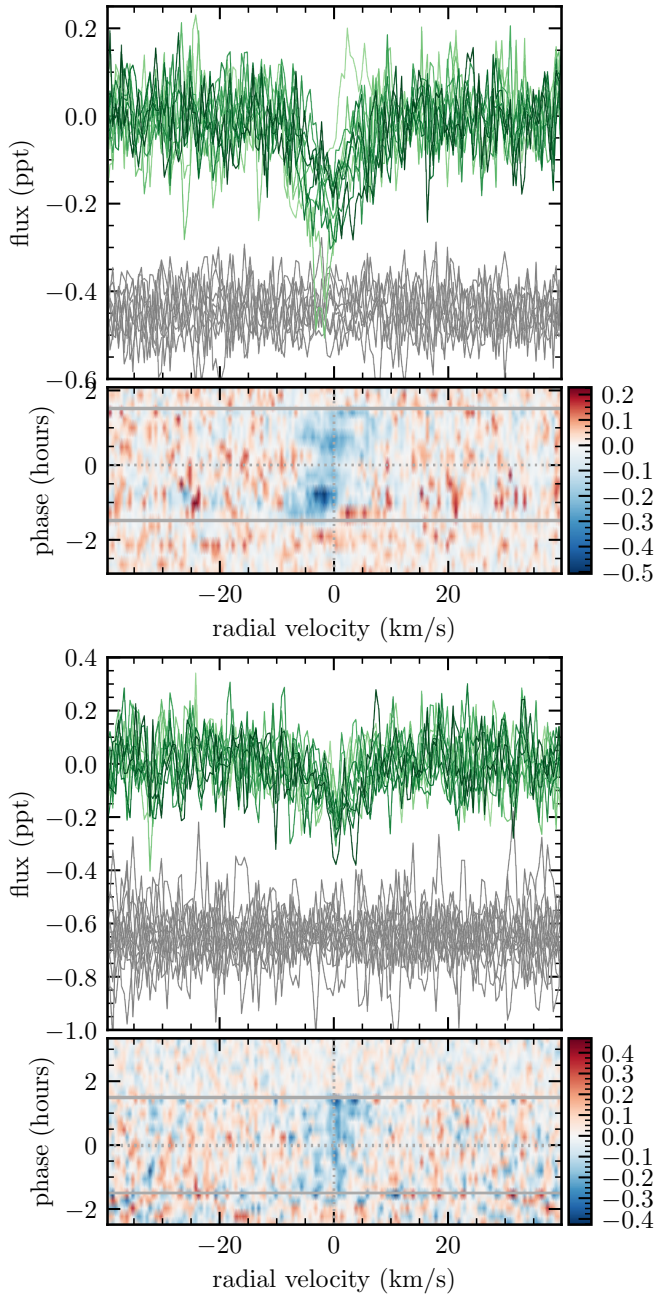


Figure 4. CCF residuals and planet traces for run A (top) and run B (bottom). In each figure, the upper panel shows the residual profiles obtained from subtracting the binned CCFs from the out of transit reference CCF (CCF_{out}). The green colours denote in-transit data, getting darker with time. The grey residuals are binned CCFs outside of transit. In the lower panels, the trace of the planet across the stellar disc is shown, where the grey solid lines denote the transit ingress and egress, while the white dotted lines denote the stellar rest velocity and transit mid-point.

not being flux-calibrated. We therefore start by normalising the DI CCFs by their individual continuum values. Moreover, we also scale them by a quadratic limb darkened transit model computed from the parameters derived in Appendix A, using the same limb darkening coefficients as in the *TESS* transit analysis. The DI CCFs are then shifted to the stellar rest frame by removing the Keplerian motion of the star due to planet c, using the semi-amplitude as derived from

Huang et al. (2018b); Gandolfi et al. (2018). The reflex motion of the star due to planet b is smaller – about 10 cm s^{-1} and 20 cm s^{-1} over the transit duration for each run, respectively – and is therefore a negligible effect. Moreover, we further shift the out-of-transit data to a common systemic velocity at each night, γ , determined from a weighted average of the out-of-transit disc-integrated radial velocities. The latter step is done in order to build as close to a true, intrinsic line profile of the star as possible, without being affected by the smearing due to the potential large radial velocity variation outside of transit, as can be seen in Fig. 2.

The signal that we are trying to extract is a very subtle distortion of the DI line profiles, which is expected to cause a shift in radial velocity of just $\sim 50 \text{ cm s}^{-1}$, or put another way; a change in the CCF shape due to the missing flux that is comparable to the transit depth of $\sim 250 \text{ ppm}$. In order to reach this precision, we are required to bin the in-transit DI CCFs to enhance the signal-to-noise of the occulted light. An additional benefit of the binning is to reduce the impact of stellar oscillations. We show in Fig. 3 the radial velocity scatter for a range of bin widths, demonstrating that the oscillations are effectively binned down as white noise for specific integration times (Chaplin et al. 2019). This is particularly clear when the observing conditions are more stable, such as for run B (Fig. B1).

While binning the DI CCFs equates to longer exposure time and thus higher SNR, it may also have detrimental effects on the signal we are trying to extract. The reloaded Rossiter-McLaughlin effect relies on isolating the differences in the DI CCF shape between in-transit and out-of-transit observations. The contrast (depth) of the DI CCF seems correlated with the SNR, as a lower SNR means fewer stellar absorption lines are resolved when cross-correlating the spectrum with the stellar template. Therefore if the contrast (or FWHM) of the in-transit DI CCFs differ from the out-of-transit DI CCFs at a comparable level to the expected missing light, the residual CCFs (that is the Doppler shadow) may be affected by this difference and thus bias the measurement of its measured radial velocity. This is particularly an issue for run A, where in Fig. B1 we show that the contrast during transit varies over a range of $\sim 500 \text{ ppm}$, which is twice the expected signal of the Doppler shadow. In order to attempt to reduce the impact of this effect, we found it best to choose a bin width large enough to effectively reduce the stellar oscillations (Fig. 3) and obtain a high enough SNR, but such that it still bins together DI CCFs with similar contrast. We found that a bin width of 15 minutes was a good compromise taking the above considerations into account, while retaining sampling.

Given the variation in contrast, we found it best to also create master out-of-transit DI CCFs that have characteristics that are as close as possible to the values of the binned in-transit DI CCFs to isolate the Doppler shadow. For each *ESPRESSO* sequence, we create three master out-of-transit CCFs that we refer to as *top*, *middle*, and *bottom*. The top and bottom master CCFs are weighted averages of a combination of the lowest and highest SNR DI CCFs, respectively. The middle master CCF is created from a combination of DI CCFs such that it falls close to the middle of the two. For each binned in-transit DI CCF we compare its contrast with that of the three master CCFs to determine which one it is closest to. From the selected master CCF we subtract the binned in-transit DI CCF to retrieve the planet-occulted residual CCFs (Doppler shadow). The residual profiles are shown in Fig. 4, where the Doppler shadow is visible in both runs. The planet appears to be progressively moving from the blueshifted hemisphere to the redshifted hemisphere, indicative of a prograde orbit.

Table 3. Priors on the Gaussian model parameters for modelling the residual CCFs. y refers to the residual CCF flux.

Parameter	Prior
A	$\mathcal{N}(0, \text{range } y)$
σ (km s ⁻¹)	$\mathcal{N}(0, 10)$
ϵ	$\mathcal{N}(0, \text{sd. } y)$
μ (km s ⁻¹)	$\mathcal{N}(0, 40)$
c	$\mathcal{N}(0, \text{sd. } y)$

2.4.2 Retrieving the surface velocities

We fit Gaussian profiles to the residual line profiles to determine the radial velocity of the surface of the star where it is occulted by the planet. In order to obtain realistic uncertainties and avoid fitting spurious signals, we use a Markov chain Monte Carlo (MCMC) sampling method to explore the full posterior distribution and propagate uncertainties in the nuisance parameters to the final radial velocity. We create our Gaussian model using `pymc3` (Salvatier et al. 2016), and vary the line centre, μ ; width, σ ; contrast, A ; and continuum level, c . Additionally, we also freely fit for the CCF error, ϵ . We use the No-U-Turn (NUTS) sampler (Hoffman & Gelman 2014) to sample the parameters from their posterior distribution. Following the procedure in Kunovac Hodžić et al. (2020), we use wide priors on our parameters related (typically related to the radial velocity grid or flux range range considered), aimed at returning a conservative estimate of the radial velocity in case the local line centre is poorly resolved. We use a half-normal prior on A , σ , and ϵ as they are restricted to positive values, and a normal prior on μ and c . The priors are shown in Table 3.

From rotational broadening of high-resolution spectra the projected rotation of π Men is estimated to be ~ 3 km s⁻¹ (Valenti & Fischer 2005). For physical reasons we therefore further restrict the value of μ to $[-5, 5]$ km s⁻¹ to avoid fitting spurious correlations that are sometimes seen outside the line core. For each residual CCF we run two individual chains for 5000 tuning steps and 1000 production steps. This typically results in >500 effective samples per parameter that are well mixed, with $\hat{R} < 1.001$ for all parameters. The fits to the individual residual line profiles are shown in Figs. C1-C6, and the derived radial velocities are shown in Fig. 5. Moreover, we show how the derived residual CCF contrast and FWHM compare between the two sequences in Fig. C7.

2.4.3 Local surface velocity modelling

We model the surface velocities following the semi-analytical model in (Cegla et al. 2016). We create a 51×51 grid that spans the size of the planet, co-moving with its centre. At every observation we compute the brightness-weighted rotational velocity by summing the cells on the stellar disc that are occulted by the planet. We assume the star follows a quadratic limb darkening law with coefficients as reported in the *TESS* analysis. We further assume the star follows rigid body rotation, as the precision of our data is not good enough to pick up latitudinal differential rotation. Similarly, we also neglect velocity contributions due to centre-to-limb convective effects. In this case, the theoretical surface velocity depends on the projected rotational velocity, $v_{\text{eq}} \sin i_{\star}$; projected spin-orbit angle, λ ; the stellar radius scaled by the planet distance, R_{\star}/a ; and orbital inclination, i_p . We vary R_{\star}/a and i_p within their Gaussian uncertainties determined from the *TESS* transit analysis (Appendix A, Table 4). We let

$v_{\text{eq}} \sin i_{\star} \sim \mathcal{U}(0, 10)$ km s⁻¹, and $\lambda \sim \mathcal{U}(-180^{\circ}, 180^{\circ})$. We sample these four parameters using the MCMC sampler as implemented in `emcee` (Foreman-Mackey et al. 2013), running 200 “walkers” for ~ 50 times the estimated autocorrelation length of the parameters. The burn-in phase is discarded by visual inspection of the timeseries of the chains, and we check that we have reached the target posterior distribution by verifying that $\hat{R} < 1.1$ for our parameters (Gelman et al. 2003). We further thin the chains by the estimated autocorrelation length, and reach >1000 effective samples per parameter. The 50th to 99th percentile of the models conditioned on the data are shown in Fig. 5. The Gaussian fit to the first residual CCF in run A (Appendix C) shows signs of a bad comparison with its out-of-transit master CCF due to the rise in flux redwards of the line centre. The line centre is measured at -4.8 km s⁻¹, which is off the scale in Fig. 5. We therefore remove the first data point from run A from our fit to being an outlier. We do however verify that our results do not change with its inclusion.

3 RESULTS

We summarise our findings from the *TESS* transit analysis, *ESPRESSO* radial velocity modelling, and reloaded Rossiter-McLaughlin analysis in Table 4. We also report the fitted values for the various Gaussian process nuisance parameters from the photometric and radial velocity analysis in Table D1. In the following, we report our main findings from the analyses presented in this paper.

3.1 Updated planet radius

We show the Gaussian process-“detrended” π Men c transit light curve in Fig. 6, which is based on a combined fit of the six available *TESS* sectors in Cycle 1. In Fig. 7 we show the transit depths from fits to individual *TESS* sectors, as well as the combined fit in grey. For comparison, we include the transit depth posteriors from Damasso et al. (2020), who also modelled the full *TESS* Cycle 1 data. Our results are consistent with the discovery papers of Huang et al. (2018b) and Gandolfi et al. (2018), and roughly consistent (1 to 2σ) to Damasso et al. (2020). The individual sectors show some spread in their distributions, and although most sectors agree to about 1σ , Sectors 11 and 8 are 2σ to 3σ discrepant from Sector 12. We attribute these differences to different timescales of correlated noise that is fit to each sector. In presence of both high- and low-frequency variation in the light curve, the Gaussian process will tend to fit the high-frequency component, which may be on a similar timescale as the transit duration, and in turn affect the derived transit depth. Given the new transit depth, we obtain a radius of π Men c, $R_p = 2.0189^{+0.047}_{-0.045} R_{\oplus}$.

3.2 Constraints on asteroseismology and the “classical” Rossiter-McLaughlin effect from radial velocity

Our Gaussian process model for stellar oscillations, variability, and Rossiter-McLaughlin effect yields a frequency of maximum oscillation power, $\nu_{\text{max}} = 2771^{+65}_{-60}$ μHz , which translates to an oscillation period of ~ 6 minutes. The longer timescale variability, ω_{bkg} , is found to be ~ 2.5 hours. From Fig. 1 we estimated $\nu_{\text{max}} \approx 2900$ μHz , but note that the visual estimate is skewed towards higher frequencies since the Nyquist frequency of run A is ~ 3000 μHz and will thus have increased power close to this frequency. The Nyquist frequency for run B is however ~ 4000 μHz and is thus sampled at a fast enough rate to resolve the true frequency.

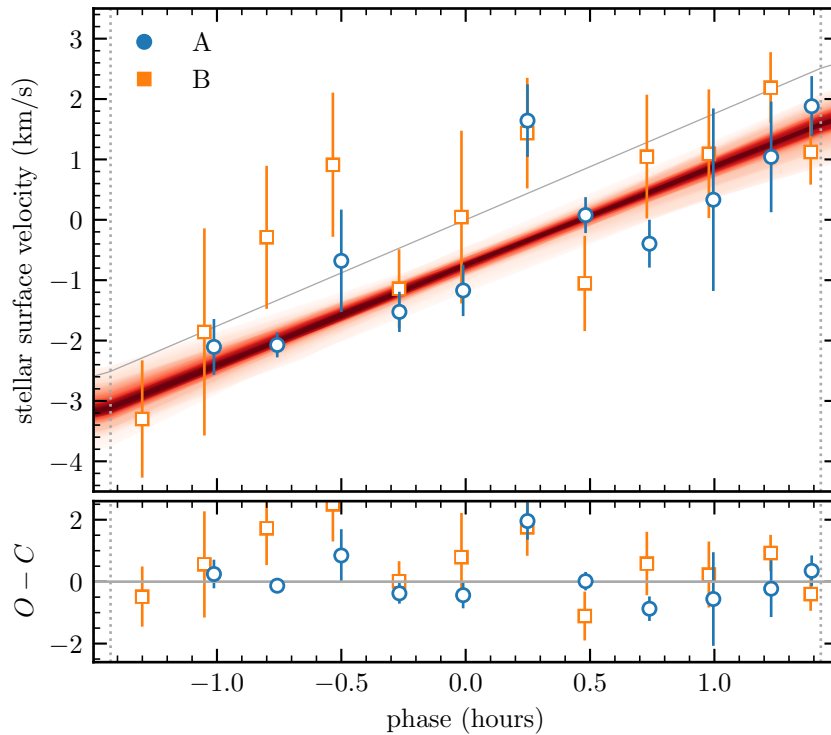


Figure 5. *Upper panel:* The local surface velocities obtained from fitting Gaussian profiles to the in-transit residual CCFs, shown as blue circles and orange squares for runs A and B, respectively. The red shaded area denote the 50th – 99th percentiles of the models generated from the posterior distribution of the fit. As a reference, the grey line denotes the $\lambda = 0^\circ$ line, which shows that alignment is firmly rejected. *Lower panel:* The residuals from the best-fitting model.

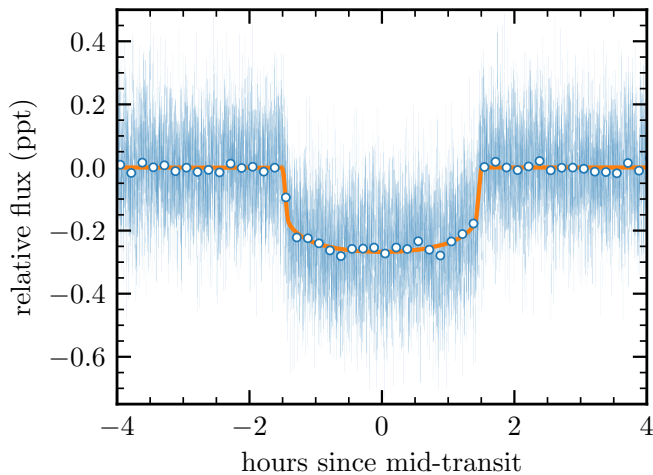


Figure 6. *TESS* data folded on the transit period after removing the best-fit Gaussian process model (*blue points*), and binned to 10 minute averages (*blue/white points*). We also show the best-fit transit model (*orange line*).

Although we do not detect Δv from the *ESPRESSO* analysis, an estimate of the surface gravity can be obtained from v_{\max} alone through the scaling relation (see [Chaplin et al. 2011](#) and references therein)

$$v_{\max} \sim 3090 \mu\text{Hz} \frac{g}{g_{\odot}} \sqrt{\frac{T_{\text{eff},\odot}}{T_{\text{eff}}}}. \quad (5)$$

This gives $\log g = 4.4018 \pm 0.0093$ and is consistent within 1σ to reported values in the discovery papers as obtained from spectral

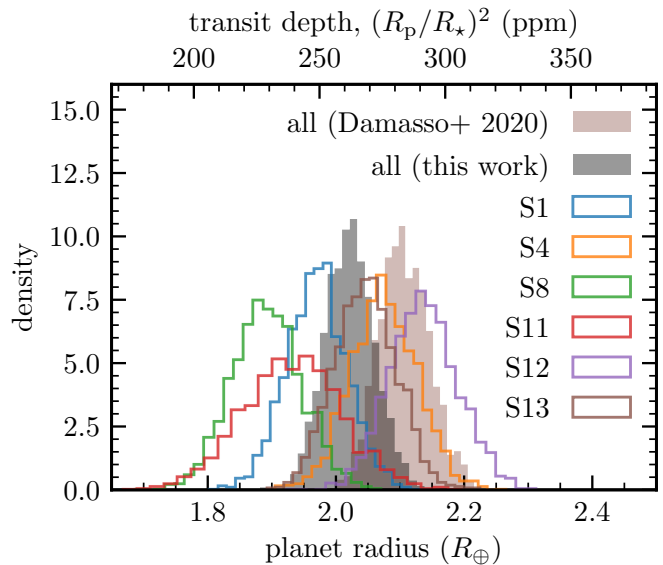


Figure 7. Comparison of the transit depth and planet radius posterior distributions from the MCMC sampling from each sector, and the full combined fit using all sectors (*gray, filled*) using a transit and Gaussian process model. We also show the posterior distribution from [Damasso et al. \(2020\)](#) (*pink, filled*) for comparison. These results are consistent with the previously reported values from [Huang et al. \(2018b\)](#) and [Gandolfi et al. \(2018\)](#).

analysis in [Ghezzi et al. \(2010\)](#), but more than a factor 3 improvement on the uncertainty.

The posterior distribution of $v_{\text{eq}} \sin i_{\star}$ shows a 2 to 3σ detec-

tion relative to 0, and a spin–orbit angle that suggests misalignment at 1σ . Based on the Bayesian Information Criterion (BIC), the Rossiter-McLaughlin model is not necessarily favoured, as the Gaussian process asteroseismic model can easily account for the expected $\sim 50 \text{ cm s}^{-1}$ variation. We test this by re-fitting the data without a Rossiter-McLaughlin model. We therefore turned to the reloaded Rossiter-McLaughlin method, where we can analyse the line profile distortions directly to detect the spectroscopic transit and measure λ .

3.3 Detection of the Doppler shadow of π Men c

The stellar surface velocities over the transit duration are plotted in Fig. 5. The two sequences follow the same overall trend, namely a positive slope for the duration of the transit as the planet moves from blueshifted to redshifted areas on the disc of the rotating star. This signature is expected for a prograde orbit, indicating the Rossiter-McLaughlin effect is detected. The combined fit to both sequences give a projected rotational velocity $v_{\text{eq}} \sin i_{\star} = 3.16 \pm 0.27 \text{ km s}^{-1}$. This value is consistent with the measurements obtained from spectroscopic line broadening in other works (Damasso et al. 2020). The offset of the model from the velocity zero-point at mid-transit determines the projected spin–orbit angle, λ . We find that the orbit is misaligned $-24^{\circ}0 \pm 4^{\circ}1$ with the stellar spin-axis. The reduced χ^2 (χ^2_{ν}) is 1.73 for the joint dataset.

We also fit the two sequences separately to check their consistency. For run A we obtain $v_{\text{eq}} \sin i_{\star} = 3.13^{+0.31}_{-0.32} \text{ km s}^{-1}$, $\lambda = -27.2^{+4.8}_{-5.3} \text{ deg}$ ($\chi^2_{\nu} = 2.19$); and for run B we get $v_{\text{eq}} \sin i_{\star} = 2.53^{+0.68}_{-0.78} \text{ km s}^{-1}$, $\lambda = -8.0^{+12.9}_{-11.6} \text{ deg}$ ($\chi^2_{\nu} = 1.53$). The joint fit is primarily driven by run A due to its higher SNR data, but $v_{\text{eq}} \sin i_{\star}$ for run B is consistent with A to 1σ , and λ to within 2σ . The lower value of λ for run B is driven by the first four points (in particular the 3rd and 4th), which are observed at low SNR compared to the second half of the transit. Fitting run B without these data gives $v_{\text{eq}} \sin i_{\star} = 3.3 \pm 0.8 \text{ km s}^{-1}$ and $\lambda = -17^{\circ} \pm 8^{\circ}$, which is more in line with run A. In Section 4.1 we discuss how the choice of master CCF may affect the parameter retrieval.

Using *Hipparcos* data of π Men, Zurlo et al. (2018) found a $18.3 \pm 1.0 \text{ d}$ periodic signal from a periodogram analysis that they interpreted as stellar rotation. Indeed, the *TESS* Sector 1 light curve show some signs of a $\sim 20 \text{ d}$ signal, which seem to have disappeared in the three month gap until π Men was observed in the next sector. We can combine the measurement of P_{rot} with R_{\star} to derive the rotational velocity, $v = 2\pi R_{\star}/P_{\text{rot}}$. We can then randomly sample from the distribution of v , and the stellar inclination, $\sin i_{\star}$, whose product can be compared to the measured $v_{\text{eq}} \sin i_{\star}$ value from the Rossiter-McLaughlin analysis to retrieve the probability distribution of i_{\star} (Masuda & Winn 2020). We carry out this exercise, but instead sample uniformly in $\cos i_{\star}$, and find that $i_{\star} = 90^{\circ}1 \pm 17^{\circ}3$. In turn, this allows us to derive the true obliquity, $\psi = 26.9^{+5.8}_{-4.7} \text{ deg}$.

4 DISCUSSION

4.1 Robustness of $v_{\text{eq}} \sin i_{\star}$ and λ

We test the robustness of our results using a number of procedures. First, we check whether our results are driven by a few points from run A that have low uncertainties, in particular the points at -1.0 h and -0.75 h and $+0.5 \text{ h}$, whose errors might be underestimated considering some of these have a low SNR disc-integrated cross-correlation function (DI CCF). We repeat our fitting procedure by excluding these

three points and find $v_{\text{eq}} \sin i_{\star} = 2.92 \pm 0.45 \text{ km s}^{-1}$, $\lambda = -23^{\circ} \pm 5^{\circ}$, which is consistent to our previous analysis.

Next, we test the sensitivity of $v_{\text{eq}} \sin i_{\star}$ and λ to our choice of fitting the residual CCF uncertainty, ϵ , to make sure the CCF uncertainties are not underestimated. We re-analyse the Gaussian fits to the residual CCFs from both runs, but this time fix the residual CCF uncertainties to the values provided by the *ESPRESSO* data products. Here we also retrieve consistent results, $v_{\text{eq}} \sin i_{\star} = 2.92 \pm 0.15 \text{ km s}^{-1}$, $\lambda = -19^{\circ} \pm 2^{\circ}$, albeit with smaller uncertainties because the fixed *ESPRESSO* CCF uncertainties are up to 30% smaller than our fitted uncertainty, ϵ . We therefore opted for the more conservative approach of fitting ϵ .

We also test how sensitive our results are to the uncertainty in the centre of the line profile. A Gaussian fit to the averaged out-of-transit disc-integrated CCFs gives an uncertainty in the radial velocity centre of $\sim 3 \text{ cm s}^{-1}$, which is below the 10 cm s^{-1} instrumental precision of *ESPRESSO*. Never the less, we repeat our analysis by perturbing the line centre velocity by $\pm 3 \text{ cm s}^{-1}$, and find that our results are not very sensitive to the line centre uncertainty, $v_{\text{eq}} \sin i_{\star} = 3.06 \pm 0.25 \text{ km s}^{-1}$, $\lambda = -19^{\circ} \pm 4^{\circ}$ and $v_{\text{eq}} \sin i_{\star} = 3.06 \pm 0.25 \text{ km s}^{-1}$, $\lambda = -24^{\circ} \pm 4^{\circ}$ (by adding and subtracting, respectively). The reduced χ^2 does however slightly increase from 1.7 to 2.3, which indicates our original solution is optimized.

It is reasonable to assume that the particular selection of spectra to build the master out-of-transit CCF in the reloaded Rossiter-McLaughlin method can impact the results. Indeed, we experimented with several ways of building the reference CCFs. Run A was particularly sensitive to this choice due to the variation in CCF shape during transit from variable observing conditions. Doing the standard approach, i.e. averaging all out-of-transit CCFs into one master CCF that is applied equally to all the binned in-transit points led to significant correlations of the retrieved surface velocities with the DI CCF contrasts. Typically the retrieved parameters using this approach would be $v_{\text{eq}} \sin i_{\star} \sim 5 \text{ km s}^{-1}$ and $\lambda \sim -50^{\circ}$ for $\chi^2_{\nu} \gg 1$. Besides the poor fit, the $v_{\text{eq}} \sin i_{\star}$ measurement was inconsistent with that determined from rotational broadening, and neither parameter was supported by the retrieved values for run B. We also attempted to build custom master CCFs for each binned in-transit CCF by selecting out-of-transit CCFs that has similar depths, within a pre-determined range. However, this approach led to the in-transit CCFs at the lowest and highest SNR/contrast (beginning and end of transit, Fig. B1) to have very few matches, which led to a low SNR master CCF. This again lead to some correlations in the retrieved surface velocities, and a solution that is inconsistent with the priors we placed on R_{\star}/a and i_p . Out of the many methods we experimented with, the method we outlined in Section 2.4.1 was the only one that led to few correlations in the surface velocities, gave $v_{\text{eq}} \sin i_{\star}$ consistent with the expectation from spectroscopic broadening, and overall less complex.

While the SNR of run B is overall lower than that of run A due to faster sampling and thus more time spent reading the CCD, the observing conditions on that night are much more stable, and gradually improve for the entire duration of the transit. This leads to a slope in the DI CCF contrast of the in-transit data that is easier to deal with. Ultimately we chose the same strategy for creating master CCFs as for run A for consistency. Overall, we found that the retrieved $v_{\text{eq}} \sin i_{\star}$ and λ for run B are less sensitive to the choice of master CCF. For example, the DI CCFs after the transit of run B have higher SNR than the pre-transit data. A more conservative – and less complex – approach for run B would be to use all the post-transit CCFs as reference. This gives $v_{\text{eq}} \sin i_{\star} \approx 3.5 \text{ km s}^{-1}$, $\lambda \approx -30^{\circ}$.

This is more consistent with the result from run A. However, due to lower SNR at the beginning of transit, this method leads to three of the residual profiles being flat. Similarly, we can also create custom master CCFs for each binned in-transit CCF as we outlined for run A in the previous paragraph. This method produces similar $v_{\text{eq}} \sin i_{\star}$, $\lambda \approx -17^{\circ}$.

Ultimately, the method of creating master CCFs should be determined based on the specific characteristics of each data set, which we have shown is different between run A and B. Adopting a less complex and conservative approach for run B (but sacrificing consistency) we obtain fully consistent results with run A, namely that the orbit of π Men c is misaligned with the stellar spin by about -30° .

4.2 Dynamical history

The formation of super-Earth and sub-Neptune multiplanetary systems is a subject of intense debate (Raymond et al. 2018; Schoonenberg et al. 2019; Coleman et al. 2019; Lee et al. 2014; Mohanty et al. 2018; Wu 2019). To this day it remains unclear whether super-Earths and sub-Neptunes form within the water iceline, or whether they can form beyond. Either, or both might be true. Detections of super-Earths in circumbinary configurations (e.g. Orosz et al. 2019; Kostov et al. 2020) point out that super-Earths can likely form at large distances before migrating inwards (Martin 2018; Pierens et al. 2020).

When proposing the observations reported here for DDT, we had initially speculated that the architecture of the π Men system was reminiscent of past dynamical interactions, and wanted to verify this with Rossiter-McLaughlin timeseries. These suspicions are now confirmed by the inclined orbital plane of the inner planet π Men c, but also thanks to three recent analyses that appeared while we were finalising our own paper. Xuan & Wyatt (2020), Damasso et al. (2020), and De Rosa et al. (2020) combined radial-velocities with *Gaia* and *Hipparcos* astrometry, and measured that π Men b is inclined with $i_b = 45^{\circ}8^{+1.4}_{-1.1}$ (Damasso et al. 2020), which also shows a large mutual inclination between π Men b and π Men c.

Together this provides evidence that super-Earths can likely form beyond the iceline around single stars. On its own, the inclination of π Men b did not imply much for π Men c. However, a natural cause for π Men c’s own orbital inclination is an exchange of angular momentum between the outer and inner planetary orbit (e.g. Wu & Lithwick 2011; Matsumura et al. 2010). Currently the two planets are likely too distant from one another to allow such an exchange. To allow raised inclinations, planet b and c would have needed to be closer. Due to their mass and angular momentum ratios, it is more likely that planet c moved inwards than for planet b to move outwards, this would imply that planet c might have formed near or beyond the iceline. Detailed N-body numerical simulations will be necessary to explore this scenario further.

5 CONCLUSION

In this paper we have presented two high-resolution spectroscopic transits of the super-Earth π Men c that we observed with *ESPRESSO*. The two timeseries show a rich concoction of signals of various origins. We perform an asteroseismic analysis on the radial velocity timeseries using Gaussian processes and clearly detect the frequency of maximum oscillation, ν_{max} . We are not sensitive to the measurement of the large frequency separation, $\Delta\nu$, and can therefore not directly measure the stellar mass and radius, but are able to obtain a much tighter constraint on $\log g$ than from spectroscopy.

We performed a transit analysis on all the available data of π Men from *TESS* Cycle 1; a total of six sectors. We revise the transit parameters for π Men c and find a radius of $R_p = 2.019^{+0.047}_{-0.045} R_{\oplus}$, which is roughly consistent with previous analyses in Damasso et al. 2020; Gandolfi et al. 2018; Huang et al. 2018b.

We attempted to fit the *ESPRESSO* radial velocity timeseries to isolate “classical”, i.e. velocimetric, Rossiter-McLaughlin effect, but the radial velocity signal was thwarted by asteroseismic p-modes and a longer term variation that we attribute to a form of stellar granulation. Instead, we turned to the reloaded Rossiter-McLaughlin method to detect the Doppler shadow. Using this method we were able to detect the transit of π Men c in spectroscopy using *ESPRESSO*, and found that its orbit is misaligned by $-24^{\circ}0 \pm 4^{\circ}1$ with the stellar spin-axis. This makes π Men c the smallest mass-ratio planet measured with the Rossiter-McLaughlin effect. Combining our results with the recent detection of the inclination of the external planet (Xuan & Wyatt 2020; Damasso et al. 2020; De Rosa et al. 2020), we speculate that π Men c likely formed at a large distance from the star. There it gravitationally interacted with π Men b, an interaction which is still evident from their mutual inclinations, π Men c’s own inclination with respect to the stellar spin axis, and the high eccentricity of π Men b.

This work stands as a testament to a new avenue of scientific investigation, namely the origins of super-Earth and sub-Neptune planets, which is now made possible by the extreme precision of *ESPRESSO*.

ACKNOWLEDGEMENTS

We would like to thank the referee for their thorough and constructive comments that substantially improved the paper. Parts of this work was carried out during a Fulbright Fellowship at the University of Chicago, funded by the U.S.–Norway Fulbright Foundation. VKH would like to thank Daniel Fabrycky and David Martin for kindly hosting him at the University of Chicago, and for useful discussions on this work. We would also like to thank Dan Foreman-Mackey for help on integrated celerite kernels and separation of kernel predictions, and Vincent Bourrier for discussions on strategies for mitigating stellar oscillations. VKH is supported by a Birmingham Doctoral Scholarship, and by a studentship from Birmingham’s School of Physics and Astronomy. This research received funding from the European Research Council (ERC) under the European Union’s Horizon 2020 research and innovation programme (grant agreement n° 803193/BEBOP and 804752/CartographyY). HMC acknowledges the financial support of the National Centre for Competence in Research PlanetS supported by the Swiss National Science Foundation (SNSF), and the UK Research Innovation Future Leaders Fellowship (MR/S035214/1). This paper includes data collected by the TESS mission. Funding for the TESS mission is provided by the NASA’s Science Mission Directorate. This research made use of exoplanet (Foreman-Mackey 2019) and its dependencies (Agol et al. 2020; Astropy Collaboration et al. 2013, 2018; Foreman-Mackey et al. 2017; Foreman-Mackey 2018; Luger et al. 2019; Salvatier et al. 2016; Team et al. 2016). This research also made use of the open-source python packages emcee (Foreman-Mackey et al. 2013), ellc (Maxted 2016), numpy (van der Walt et al. 2011), scipy (Jones et al. 2002), and matplotlib (Hunter 2007).

DATA AVAILABILITY

The spectroscopic data underlying this article are available from the public ESO archive². The photometric data are publicly available from the Mikulski Archive for Space Telescopes (MAST) portal.³

REFERENCES

- Addison B. C., et al., 2020, arXiv e-prints, 2006, arXiv:2006.13675
- Agol E., Luger R., Foreman-Mackey D., 2020, *The Astronomical Journal*, 159, 123
- Albrecht S., Reffert S., Snellen I., Quirrenbach A., Mitchell D. S., 2007, *Astronomy and Astrophysics*, 474, 565
- Angus R., Morton T., Aigrain S., Foreman-Mackey D., Rajpaul V., 2018, *Monthly Notices of the Royal Astronomical Society*, 474, 2094
- Armitage P. J., 2013, *Astrophysics of Planet Formation*
- Astropy Collaboration et al., 2013, *Astronomy and Astrophysics*, 558, A33
- Astropy Collaboration et al., 2018, *The Astronomical Journal*, 156, 123
- Barclay T., Pepper J., Quintana E. V., 2018, *The Astrophysical Journal Supplement Series*, 239, 2
- Baruteau C., et al., 2014, *Protostars and Planets VI*, p. 667
- Batalha N. M., et al., 2013, *The Astrophysical Journal Supplement Series*, 204, 24
- Bitsch B., Crida A., Libert A.-S., Lega E., 2013, *Astronomy and Astrophysics*, 555, A124
- Bonfils X., et al., 2013, *Astronomy and Astrophysics*, 549, A109
- Borucki W. J., et al., 2010, *Science*, 327, 977
- Bourrier V., Hébrard G., 2014, *Astronomy and Astrophysics*, 569, A65
- Bourrier V., Cegla H. M., Lovis C., Wyttenbach A., 2017, *Astronomy and Astrophysics*, 599, A33
- Bourrier V., et al., 2018, *Nature*, 553, 477
- Cegla H. M., Lovis C., Bourrier V., Beeck B., Watson C. A., Pepe F., 2016, *Astronomy and Astrophysics*, 588, A127
- Chabrier G., Johansen A., Janson M., Rafikov R., 2014, *Protostars and Planets VI*, pp 619–642
- Chaplin W. J., et al., 2011, *The Astrophysical Journal*, 732, 54
- Chaplin W. J., Cegla H. M., Watson C. A., Davies G. R., Ball W. H., 2019, *The Astronomical Journal*, 157, 163
- Chatterjee S., Ford E. B., Matsumura S., Rasio F. A., 2008, *The Astrophysical Journal*, 686, 580
- Coleman G. A. L., Leleu A., Alibert Y., Benz W., 2019, *Astronomy and Astrophysics*, 631, A7
- Collier Cameron A., Bruce V. A., Miller G. R. M., Triaud A. H. M. J., Queloz D., 2010, *Monthly Notices of the Royal Astronomical Society*, 403, 151
- Damasso M., et al., 2020, arXiv e-prints, 2007, arXiv:2007.06410
- Dawson R. I., 2014, *The Astrophysical Journal*, 790, L31
- Dawson R. I., Lee E. J., Chiang E., 2016, *The Astrophysical Journal*, 822, 54
- De Rosa R. J., Dawson R., Nielsen E. L., 2020, arXiv e-prints, 2007, arXiv:2007.08549
- Dressing C. D., Charbonneau D., 2015, *The Astrophysical Journal*, 807, 45
- Ehrenreich D., et al., 2020, *Nature*, 580, 597
- Fabrycky D., Tremaine S., 2007, *The Astrophysical Journal*, 669, 1298
- Farr W. M., et al., 2018, *The Astrophysical Journal*, 865, L20
- Foreman-Mackey D., 2018, *Research Notes of the American Astronomical Society*, 2, 31
- Foreman-Mackey D., 2019, *Astrophysics Source Code Library*, p. ascl:1910.005
- Foreman-Mackey D., Hogg D. W., Lang D., Goodman J., 2013, *Publications of the Astronomical Society of the Pacific*, 125, 306
- Foreman-Mackey D., Agol E., Ambikasaran S., Angus R., 2017, *The Astronomical Journal*, 154, 220
- Fressin F., et al., 2013, *The Astrophysical Journal*, 766, 81
- Gaia Collaboration et al., 2018, *Astronomy and Astrophysics*, 616, A1
- Gaidos E., Mann A. W., Kraus A. L., Ireland M., 2016, *Monthly Notices of the Royal Astronomical Society*, 457, 2877
- Gandolfi D., et al., 2018, *Astronomy and Astrophysics*, 619, L10
- Gelman A., Carlin J. B., Stern H. S., Rubin D. B., 2003, *Bayesian Data Analysis*, Second Edition. CRC Press
- Ghezzi L., Cunha K., Smith V. V., de Araújo F. X., Schuler S. C., de la Reza R., 2010, *The Astrophysical Journal*, 720, 1290
- Gillen E., Hillenbrand L. A., David T. J., Aigrain S., Rebull L., Stauffer J., Cody A. M., Queloz D., 2017, *The Astrophysical Journal*, 849, 11
- Grunblatt S. K., Howard A. W., Haywood R. D., 2015, *The Astrophysical Journal*, 808, 127
- Hansen B. M. S., Murray N., 2012, *The Astrophysical Journal*, 751, 158
- Hardegree-Ullman K. K., Cushing M. C., Muirhead P. S., Christiansen J. L., 2019, *The Astronomical Journal*, 158, 75
- Harvey J., 1985, in Rolfe E., Battrick B., eds, *ESA Special Publication Vol. 235, Future Missions in Solar, Heliospheric & Space Plasma Physics*. p. 199
- Haywood R. D., et al., 2014, *Monthly Notices of the Royal Astronomical Society*, 443, 2517
- Hirano T., Narita N., Shporer A., Sato B., Aoki W., Tamura M., 2011, *Publications of the Astronomical Society of Japan*, 63, 531
- Hirano T., et al., 2020, *The Astrophysical Journal Letters*, 899, L13
- Hoffman M. D., Gelman A., 2014, *Journal of Machine Learning Research*, 15, 1593
- Howard A. W., et al., 2010, *Science*, 330, 653
- Huang C. X., et al., 2018a, arXiv e-prints, p. arXiv:1807.11129
- Huang C. X., et al., 2018b, *The Astrophysical Journal Letters*, 868, L39
- Hunter J. D., 2007, *Computing in Science Engineering*, 9, 90
- Johansen A., Lambrechts M., 2017, *Annual Review of Earth and Planetary Sciences*, 45, 359
- Jones H. R. A., Paul Butler R., Tinney C. G., Marcy G. W., Penny A. J., McCarthy C., Carter B. D., Pourbaix D., 2002, *Monthly Notices of the Royal Astronomical Society*, 333, 871
- Kipping D. M., 2013, *Monthly Notices of the Royal Astronomical Society*, 434, L51
- Kostov V. B., et al., 2020, arXiv e-prints, 2004, arXiv:2004.07783
- Kunovac-Hodžić V., Triaud A., 2019, *AAS - Extreme Solar Systems IV*, 4, 308.01
- Kunovac Hodžić V., et al., 2020, arXiv e-prints, 2007, arXiv:2007.05514
- Lambrechts M., Morbidelli A., Jacobson S. A., Johansen A., Bitsch B., Izidoro A., Raymond S. N., 2019, *Astronomy and Astrophysics*, 627, A83
- Lee E. J., Chiang E., Ormel C. W., 2014, *The Astrophysical Journal*, 797, 95
- Lightkurve Collaboration et al., 2018, *Astrophysics Source Code Library*, p. ascl:1812.013
- López-Morales M., et al., 2014, *The Astrophysical Journal*, 792, L31
- Luger R., Agol E., Foreman-Mackey D., Fleming D. P., Lustig-Yaeger J., Deitrick R., 2019, *The Astronomical Journal*, 157, 64
- Martin D. V., 2018, *Handbook of Exoplanets*, p. 156
- Masuda K., Winn J. N., 2020, *The Astronomical Journal*, 159, 81
- Matsumura S., Thommes E. W., Chatterjee S., Rasio F. A., 2010, *The Astrophysical Journal*, 714, 194
- Macted P. F. L., 2016, *Astronomy and Astrophysics*, 591, A111
- Mayor M., et al., 2011, arXiv e-prints, 1109, arXiv:1109.2497
- McLaughlin D. B., 1924, *The Astrophysical Journal*, 60, 22
- Mohanty S., Jankovic M. R., Tan J. C., Owen J. E., 2018, *The Astrophysical Journal*, 861, 144
- Naoz S., Farr W. M., Lithwick Y., Rasio F. A., Teyssandier J., 2011, *Nature*, 473, 187
- Orosz J. A., et al., 2019, *The Astronomical Journal*, 157, 174
- Paardekooper S.-J., Leinhardt Z. M., Thébault P., Baruteau C., 2012, *The Astrophysical Journal Letters*, 754, L16
- Palle E., et al., 2020, *Astronomy and Astrophysics*, 643, A25
- Pepe F., et al., 2014, *Astronomische Nachrichten*, 335, 8
- Pierens A., McNally C. P., Nelson R. P., 2020, *Monthly Notices of the Royal Astronomical Society*, 496, 2849
- Pollack J. B., Hubickyj O., Bodenheimer P., Lissauer J. J., Podolak M., Greenzweig Y., 1996, *Icarus*, 124, 62

² www.archive.eso.org

³ <https://mast.stsci.edu/portal/Mashup/Clients/Mast/Portal.html>

Table 4. System parameters for π Men (HD 39091) and derived planet parameters from the *ESPRESSO* and *TESS* analysis. ^aDetermined from spectral broadening. ^bFixed. ^cDerived from v_{\max} using Equation 5. ^dDerived from the combination of P_{rot} , R_{\star} , and $v_{\text{eq}} \sin i_{\star}$.

Parameter	Description	Value	Reference/data
<i>System information and stellar parameters</i>			
<i>Gaia</i> DR2 ID	–	4623036865373793408	Simbad
<i>TIC</i>	<i>TESS</i> Input Catalog ID	261136679	MAST
α	Right ascension	5 ^h 37 ^m 9 ^s .89	Simbad
δ	Declination	−80°28′8″.8	Simbad
<i>V</i> (mag)	Apparent magnitude	5.67	Simbad
Distance (pc)	Parallax distance	18.27 ± 0.02	Gaia Collaboration et al. (2018)
T_{eff} (K)	Effective temperature	5998 ± 62	Damasso et al. (2020)
log <i>g</i> (cgs)	Stellar surface gravity	4.43 ± 0.1	Damasso et al. (2020)
[Fe/H] (dex)	Stellar metallicity	0.09 ± 0.04	Damasso et al. (2020)
$v_{\text{eq}} \sin i_{\star}$ (km s ^{−1})	Projected rotational velocity	3.34 ± 0.07 ^a	Damasso et al. (2020)
M_{\star} (M_{\odot})	Stellar mass	1.07 ± 0.04	Damasso et al. (2020)
R_{\star} (R_{\odot})	Stellar radius	1.17 ± 0.02	Damasso et al. (2020)
L_{\star} (L_{\odot})	Stellar luminosity	1.44 ± 0.02	Huang et al. (2018b)
τ_{\star} (Gyr)	Stellar age	2.98 ^{+1.4} _{−1.3}	Huang et al. (2018b)
P_{rot} (days)	Photometric rotation period	18.3 ± 1.0	Zurlo et al. (2018)
<i>Transit parameters</i>			
<i>P</i> (days)	Orbital period	6.2678399 ± 0.000011	<i>TESS</i>
T_0 (BJD _{UTC} − 2 450 000)	Transit mid-point	8425.789204 ^{+0.000279} _{−0.000280}	<i>TESS</i>
R_p (R_{\oplus})	Planet radius	2.0189 ^{+0.0465} _{−0.0448}	<i>TESS</i>
R_p/R_{\star}	Planet-to-star radius ratio	0.015844 ^{+0.000139} _{−0.000136}	<i>TESS</i>
DT_0 (ppm)	Transit depth at T_0	267.59 ^{+4.16} _{−3.89}	<i>TESS</i>
R_{\star}/a	Scaled separation	0.07978 ^{+0.00175} _{−0.00172}	<i>TESS</i>
b (R_{\star})	Impact parameter	0.6465 ^{+0.0191} _{−0.0210}	<i>TESS</i>
i_p (°)	Orbital inclination	87.045 ^{+0.157} _{−0.156}	<i>TESS</i>
T_{14} (days)	Transit duration between 1 st and 4 th contacts	0.125001 ^{+0.000484} _{−0.000464}	<i>TESS</i>
e	Eccentricity	0 ^b	<i>TESS</i>
ω (°)	Argument of periastron	0 ^b	<i>TESS</i>
<i>“Classical” Rossiter-McLaughlin and asteroseismology</i>			
$v_{\text{eq}} \sin i_{\star}$ (km s ^{−1})	Projected rotation velocity	4.29 ^{+1.57} _{−1.58}	<i>ESPRESSO</i> RVs
λ (°)	Spin–orbit angle	−20.4 ^{+26.4} _{−24.6}	<i>ESPRESSO</i> RVs
ν_{\max} (μHz)	Frequency of maximum oscillation	2771.2 ^{+65.3} _{−59.9}	<i>ESPRESSO</i> RVs
log <i>g</i> (cgs)	Stellar surface gravity ^c	4.4018 ± 0.0093	<i>ESPRESSO</i> RVs
<i>Reloaded Rossiter-McLaughlin</i>			
$v_{\text{eq}} \sin i_{\star}$ (km s ^{−1})	Projected rotational velocity (run A,B)	3.16 ± 0.27	<i>ESPRESSO</i> CCFs
λ (°)	Projected spin–orbit angle (run A,B)	−24.0 ± 4.1	<i>ESPRESSO</i> CCFs
i_{\star} (°)	Stellar inclination ^d	90.1 ± 17.3	P_{rot} , R_{\star} , $v_{\text{eq}} \sin i_{\star}$
ψ (°)	3D spin–orbit angle ^d	26.9 ^{+5.8} _{−4.7}	λ , i_p , i_{\star}

Press W. H., Rybicki G. B., 1989, *The Astrophysical Journal*, 338, 277
Raymond S. N., Boulet T., Izidoro A., Esteves L., Bitsch B., 2018, *Monthly Notices of the Royal Astronomical Society*, 479, L81
Ricker G. R., et al., 2015, *Journal of Astronomical Telescopes, Instruments, and Systems*, 1, 014003
Rossiter R. A., 1924, *The Astrophysical Journal*, 60, 15
Salvatier J., Wiecki T. V., Fonnesbeck C., 2016, *PeerJ Computer Science*, 2, e55
Schlichting H. E., 2014, *The Astrophysical Journal*, 795, L15
Schlichting H. E., 2018, [arXiv:1802.03090 \[astro-ph\]](#) 10.1007/978-3-319-30648-3_141-1, pp 1–20
Schoonenberg D., Liu B., Ormel C. W., Dorn C., 2019, *Astronomy and*

Astrophysics, 627, A149
Team T. T. D., et al., 2016, [arXiv:1605.02688 \[cs\]](#)
Triard A. H. M. J., 2018, *Handbook of Exoplanets*, p. 2
Valenti J. A., Fischer D. A., 2005, *The Astrophysical Journal Supplement Series*, 159, 141
Winn J. N., et al., 2010a, *The Astrophysical Journal*, 718, 575
Winn J. N., Fabrycky D., Albrecht S., Johnson J. A., 2010b, *The Astrophysical Journal*, 718, L145
Wu Y., 2019, *The Astrophysical Journal*, 874, 91
Wu Y., Lithwick Y., 2011, *The Astrophysical Journal*, 735, 109
Xuan J. W., Wyatt M. C., 2020, *Monthly Notices of the Royal Astronomical Society*

Zurlo A., et al., 2018, *Monthly Notices of the Royal Astronomical Society*, 480, 35

van der Walt S., Colbert S. C., Varoquaux G., 2011, *Computing in Science and Engineering*, 13, 22

APPENDIX A: TESS PHOTOMETRIC ANALYSIS

The most recent published orbital parameters for π Men c are based on an analysis of *TESS* Sector 1 data (Huang et al. 2018b; Gandolfi et al. 2018), with respectively 5 and 7 minute uncertainties on the ephemerides at the time of our spectroscopic transits. Moreover, the initial analyses did not take into account correlated noise in their modelling, which may lead to underestimated errors on the reported transit parameters and can impact our Rossiter-McLaughlin modelling. The light curve from Sector 1 may also show evidence of rotational modulation from a spot on the stellar surface, which may bias the measurement of the transit depth to higher values and thus overestimate the Rossiter-McLaughlin amplitude.

π Men is in a region of the sky that is being overlapped by several *TESS* sectors while the spacecraft surveyed the Southern Hemisphere in Cycle 1, which has since completed. π Men has been observed in Sectors 1 (25 July – 22 August 2018); 4 (18 October – 15 November 2018); 8 (2 – 28 February 2019), 11 (22 April – 21 May 2019), 12 (21 May – 19 June 2019); and 13 (19 June – 18 July 2019). In this section we outline our light curve modelling including the five remaining *TESS* sectors that were not yet available in the discovery papers, and take into account correlated noise using a Gaussian process model coupled to a transit model.

A1 Flux extraction and pixel-level decorrelation

The *TESS* 2-minute cadence Target Pixel Files (TPF) for sectors 1, 4, 8, 11, 12, and 13 were downloaded using the `LIGHTKURVE` package (Lightkurve Collaboration et al. 2018). We performed simple aperture photometry using the optimal aperture as determined by the *TESS* Science Processing Operations Center (SPOC). Using this aperture, the relative contribution from contaminant flux in our target aperture is of the order 0.3 ppt, which has a negligible impact (~ 10 ppm) on the transit signals.

The raw light curves have systematic effects from the instrument and telescope motion, in particular at the beginning and ends of each *TESS* orbit. In order to remove these effects we applied pixel-level decorrelation (PLD) on the raw light curves using the first order PLD basis and the top principal components from the second order basis. In this work we opted for an implementation as detailed in the documentation for the `exoplanet`⁴ package (Foreman-Mackey 2019), but a similar more flexible version can be found in the `LIGHTKURVE`⁵ package as well.

A2 Transit light curve modelling of *TESS* sectors 1, 4, 8, 11, 12, 13

We used the `exoplanet` software package (Foreman-Mackey 2019) to model the *TESS* transit signals, including a correlated noise model using Gaussian process regression with `celerite` (Foreman-Mackey et al. 2017). We assumed the star follows a quadratic limb darkening law and held the limb darkening parameters $c_1 = 0.28$, $c_2 = 0.27$

fixed for the *TESS* band, following (Huang et al. 2018b). We fit for the orbital period, P ; transit midpoint, T_0 ; impact parameter, b ; and planet radius, $\ln r_p$, while also sampling the stellar radius and mass with normal priors $R_\star = 1.17 \pm 0.02 R_\odot$, $M_\star = 1.07 \pm 0.04 M_\odot$ from the analysis in (Damasso et al. 2020).

For our Gaussian process model we used a kernel with covariance function given by

$$k(\tau) = \sigma^2 \left[(1 - 1/\epsilon) \exp\left(-\frac{1 - \epsilon}{\rho} \sqrt{3}\tau\right) (1 - 1/\epsilon) \exp\left(-\frac{1 + \epsilon}{\rho} \sqrt{3}\tau\right) \right]$$

where σ describes the amplitude of the signal, and ρ is a characteristic timescale. In the limit $\epsilon \rightarrow 0$ the above function becomes the Matérn-3/2 function, which can flexibly fit instrument systematics related to the *TESS* pointing as well as some astrophysical variability, although the light curves seem to be dominated by the former. We use the default setting in `celerite` to approximate the Matérn-3/2 function ($\epsilon = 0.01$), and fit for the logarithm of the amplitude, $\ln \sigma$, and logarithm of the timescale, $\ln \rho$. Finally, we also fit for the logarithm of a white noise term for our photometric uncertainties, $\ln s^2$, as well as a photometric offset, Δf . Since each *TESS* sector has different noise properties, we fit each of the above nuisance parameters separately for each sector, while the transit parameters are shared between the full dataset. The full set of priors used in the analysis is shown in Table A1.

We found that the measurement of a consistent transit depth between *TESS* sectors is very sensitive to the timescale of the baseline model being fit. Even after the PLD correction, some data show somewhat disjoint 2.5 day segments from “momentum dumps” as thrusters are fired to reorient the *TESS* spacecraft, pointing drifts at the start and/or end of each *TESS* orbit, and other show timescale variation that is most likely related to the spacecraft pointing. In an otherwise smoothly varying light curve, these “rapid” changes drive the timescale of the Gaussian process kernel lower values to be able to fit both high and low frequency variation, which will affect the transit depth. In order to avoid biasing the measurement of the transit depth, we remove some out-of-transit segments of data associated with rapid changes in the light curve, which range from a few hours to a few days. In addition, one transit from Sector 11 is removed due to a momentum dump during transit that is not sufficiently corrected from the PLD.

We first fit the data using a least squares algorithm to find the maximum likelihood, and performed a single 5σ -clip on the residuals from the best-fitting model to remove outliers. We then sampled the free parameters of our model with Markov Chain Monte Carlo using the No-U-Turn (NUTS) sampler (Hoffman & Gelman 2014) as implemented in `pymc3` (Salvatier et al. 2016) and `exoplanet`. We launched four independent chains, discarded the first 2000 tuning steps, and finally sampled 1000 additional steps, resulting in >1000 effective samples per parameter. All parameters reached the recommended $\hat{R} < 1.1$ (typically < 1.001) convergence criterion (Gelman et al. 2003). We performed the MCMC sampling individually for each *TESS* sector, and also using the full combined dataset. The baseline-corrected, phase-folded transit light curve is shown in Fig. 6, and the full transit and Gaussian process fit to the data is shown in Fig. A1 with residual rms scatter of 123 ppm.

We also searched for transit timing variations (TTVs) by fitting individual transit times, but found no significant signal. Finally, we also searched the combined *TESS* residual light curve for solar-like oscillations, but were unable to uncover evidence of detectable modes. However, as we report in Section 2, the high S/N *ESPRESSO* data do show clearly detectable oscillations in Doppler velocity.

⁴ exoplanet.dfm.io

⁵ <http://docs.lightkurve.org>

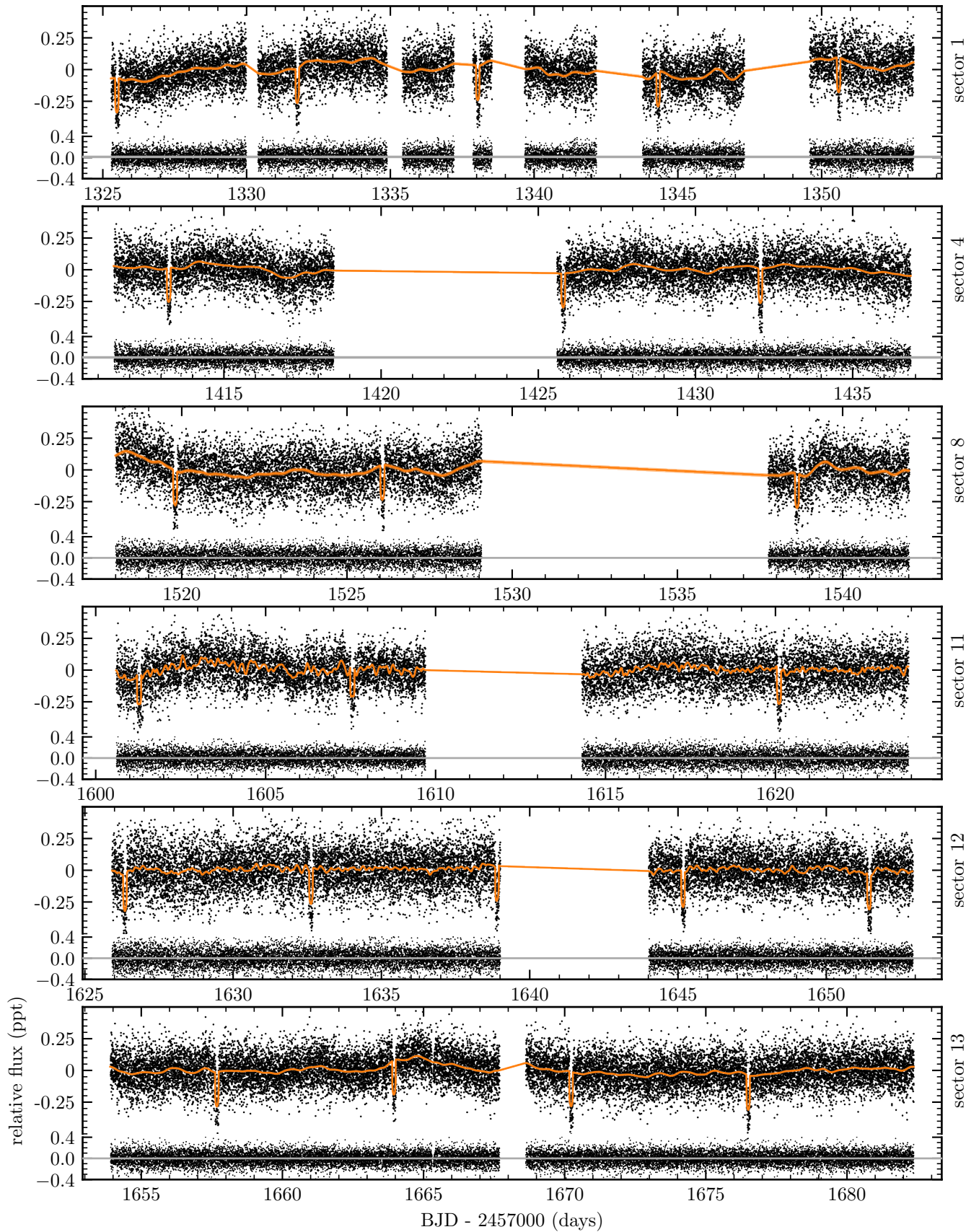


Figure A1. *TESS* data (black points) from sectors 1, 4, 8, 11, 12, and 13 fitted with the Gaussian process model and transit model (orange line) described in Section A. In the lower panel of each sector we show the residuals from the best fit.

Table A1. Priors on the parameters for the photometric transit modelling. N refers to individual sectors. ^a Impact parameter prior (Beta distribution) from Kipping (2013).

Parameter	Prior
$M_\star (M_\odot)$	$\mathcal{N}(1.07, 0.04)$
$R_\star (R_\odot)$	$\mathcal{N}(1.17, 0.02)$
$\ln r_p (R_\odot)$	$\mathcal{N}(-4.05, 1)$
$\ln P$ (days)	$\mathcal{N}(1.84, 1)$
T_0 (BJD-2 450 000)	$\mathcal{N}(8425.7892, 1)$
b	\mathcal{B}^a
$\ln \sigma_N$	$\mathcal{N}(\ln \text{var } y_N, 10)$
$\ln \rho_N$	$\mathcal{N}(0, 10)$
$\ln s_N^2$	$\mathcal{N}(\ln \text{var } y_N, 10)$
Δf_N	$\mathcal{N}(1, 0.1)$

APPENDIX B: ESPRESSO OBSERVABLES

APPENDIX C: RESIDUAL CCF PROFILES

APPENDIX D: GAUSSIAN PROCESS HYPERPARAMETERS

This paper has been typeset from a $\text{\TeX}/\text{\LaTeX}$ file prepared by the author.

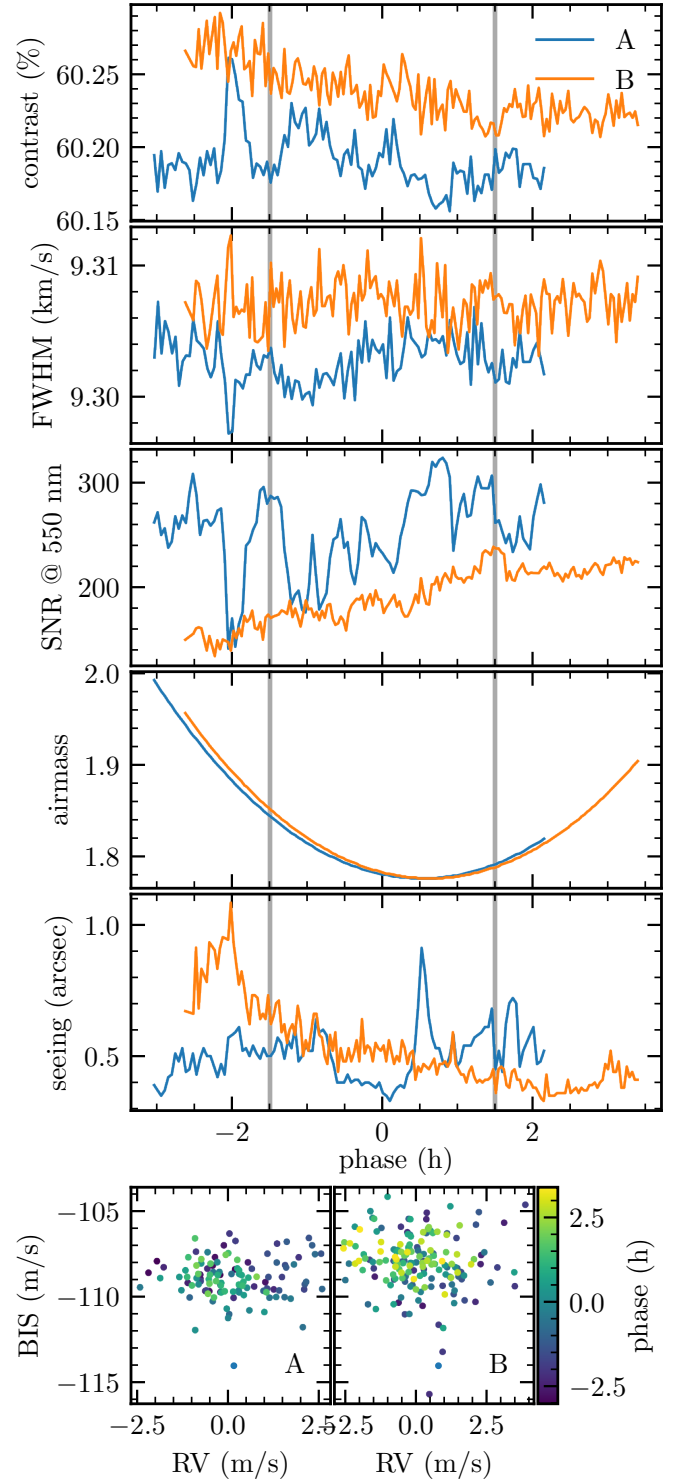


Figure B1. Observing conditions and CCF observables for *ESPRESSO* run A (blue) and run B (orange). From top to bottom: CCF contrast, CCF FWHM, SNR at 550 nm, airmass, seeing, and bisector inverse slope (BIS). The grey vertical lines denote the transit ingress and egress.

Table D1. Table of Gaussian process hyperparameters from the photometric and radial velocity analysis.

Parameter	Description	Value	Source
<i>Photometric analysis</i>			
<i>Sector 1</i>			
$\log \sigma$	Gaussian process amplitude	$-0.44^{+0.18}_{-0.17}$	TESS
$\log \rho$	Gaussian process timescale	$-9.93^{+0.16}_{-0.13}$	TESS
$\log s^2$	Flux variance	$-18.037^{+0.012}_{-0.012}$	TESS
Δf	Mean flux	$1.0000054^{+0.0000111}_{-0.0000123}$	TESS
<i>Sector 4</i>			
$\log \sigma$	Gaussian process amplitude	$-0.58^{+0.25}_{-0.26}$	TESS
$\log \rho$	Gaussian process timescale	$-10.47^{+0.16}_{-0.14}$	TESS
$\log s^2$	Flux variance	$-18.169^{+0.013}_{-0.012}$	TESS
Δf	Mean flux	$0.9999993^{+0.0000078}_{-0.0000078}$	TESS
<i>Sector 8</i>			
$\log \sigma$	Gaussian process amplitude	$-0.47^{+0.26}_{-0.23}$	TESS
$\log \rho$	Gaussian process timescale	$-9.95^{+0.18}_{-0.16}$	TESS
$\log s^2$	Flux variance	$-17.903^{+0.013}_{-0.014}$	TESS
Δf	Mean flux	$1.0000088^{+0.0000134}_{-0.0000139}$	TESS
<i>Sector 11</i>			
$\log \sigma$	Gaussian process amplitude	$-2.63^{+0.15}_{-0.14}$	TESS
$\log \rho$	Gaussian process timescale	$-10.26^{+0.06}_{-0.06}$	TESS
$\log s^2$	Flux variance	$-18.083^{+0.012}_{-0.013}$	TESS
Δf	Mean flux	$1.0000049^{+0.0000034}_{-0.0000033}$	TESS
<i>Sector 12</i>			
$\log \sigma$	Gaussian process amplitude	$-2.52^{+0.28}_{-0.25}$	TESS
$\log \rho$	Gaussian process timescale	$-10.71^{+0.08}_{-0.08}$	TESS
$\log s^2$	Flux variance	$-17.873^{+0.012}_{-0.011}$	TESS
Δf	Mean flux	$1.0000128^{+0.0000023}_{-0.0000023}$	TESS
<i>Sector 13</i>			
$\log \sigma$	Gaussian process amplitude	$-0.64^{+0.23}_{-0.24}$	TESS
$\log \rho$	Gaussian process timescale	$-10.41^{+0.12}_{-0.11}$	TESS
$\log s^2$	Flux variance	$-18.211^{+0.011}_{-0.010}$	TESS
Δf	Mean flux	$1.0000019^{+0.0000062}_{-0.0000060}$	TESS
<i>Radial velocity analysis</i>			
$\log S_{\text{osc}} (\text{km}^2 \text{s}^{-2})$	Oscillation power	$-22.58^{+0.21}_{-0.27}$	ESPRESSO RVs
$\log Q_{\text{osc}}$	Oscillation damping	$1.58^{+0.23}_{-0.21}$	ESPRESSO RVs
$\log S_{\text{bkg}} (\text{km}^2 \text{s}^{-2})$	Background activity power	$-18.48^{+0.90}_{-0.68}$	ESPRESSO RVs
$\log \omega_{\text{bkg}} (\text{d}^{-1})$	Background activity timescale	$4.07^{+0.32}_{-0.34}$	ESPRESSO RVs
$\log \sigma_{\text{A}} (\text{km s}^{-1})$	White noise term for run A	$-10.31^{+1.25}_{-1.16}$	ESPRESSO RVs
$\log \sigma_{\text{B}} (\text{km s}^{-1})$	White noise term for run B	$-8.29^{+0.67}_{-2.35}$	ESPRESSO RVs

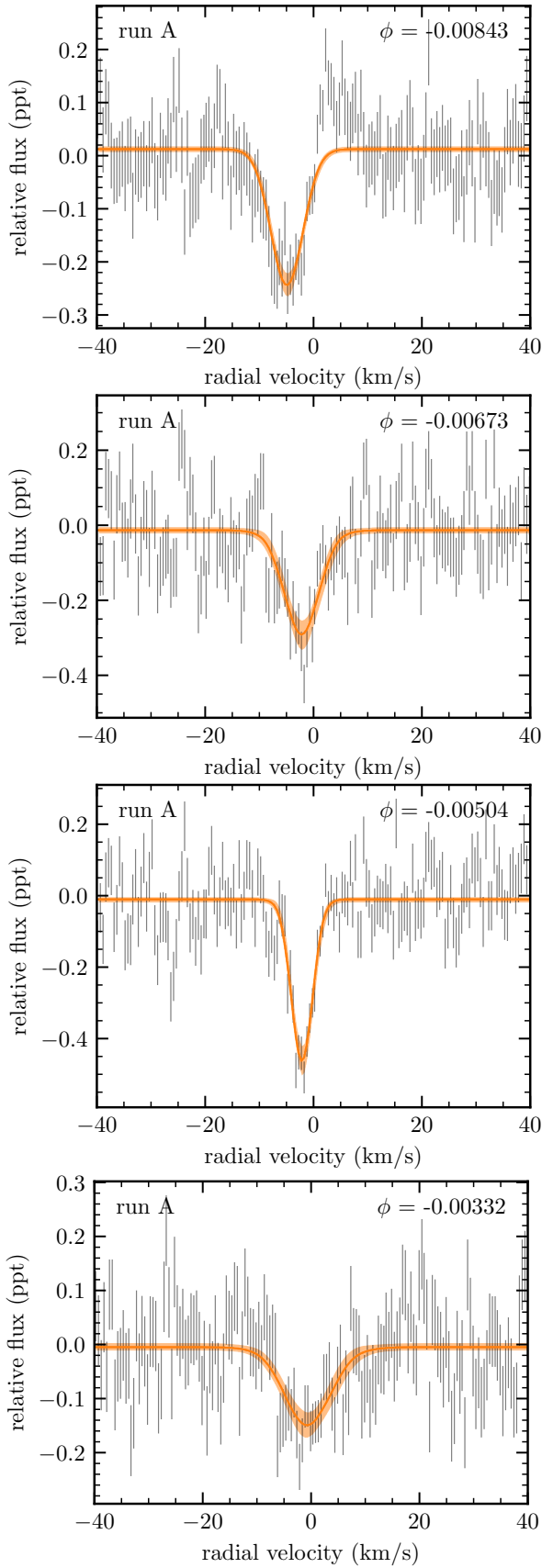


Figure C1. Gaussian fits to the 15 min binned residual line profiles from run A. The orange shading denotes the 1σ uncertainty of the model.

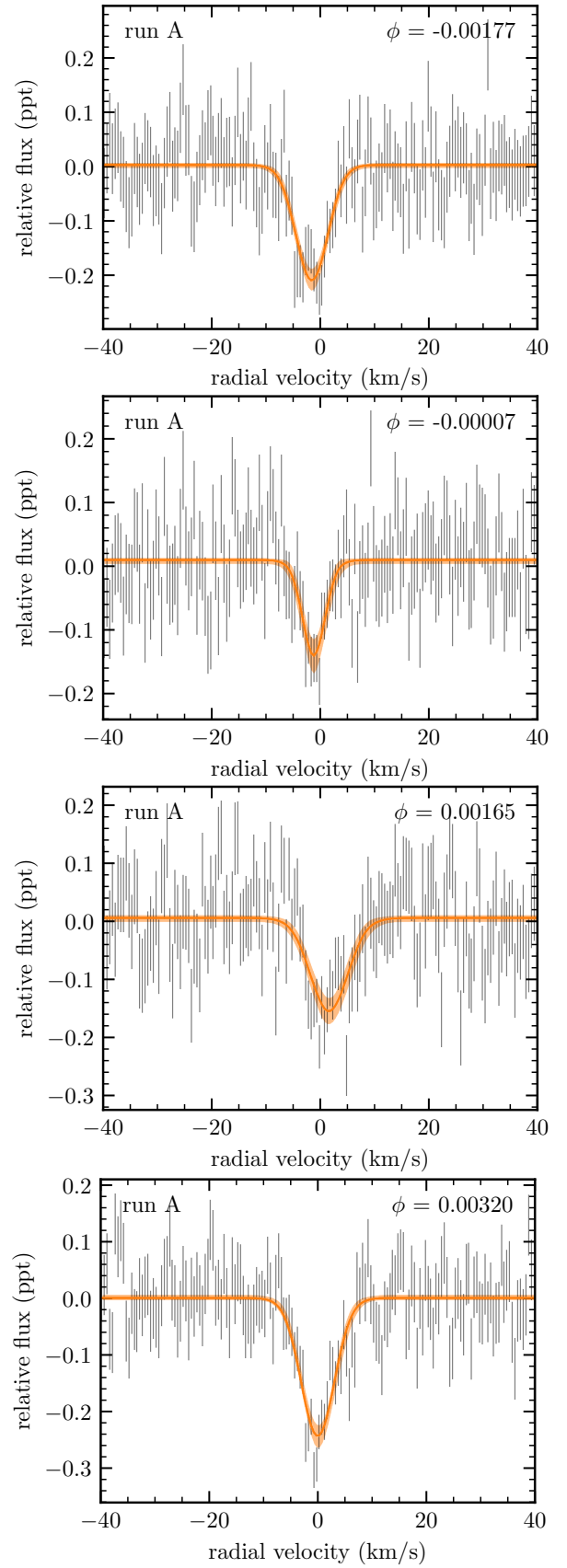


Figure C2. Gaussian fits to the 15 min binned residual line profiles from run A. The orange shading denotes the 1σ uncertainty of the model.

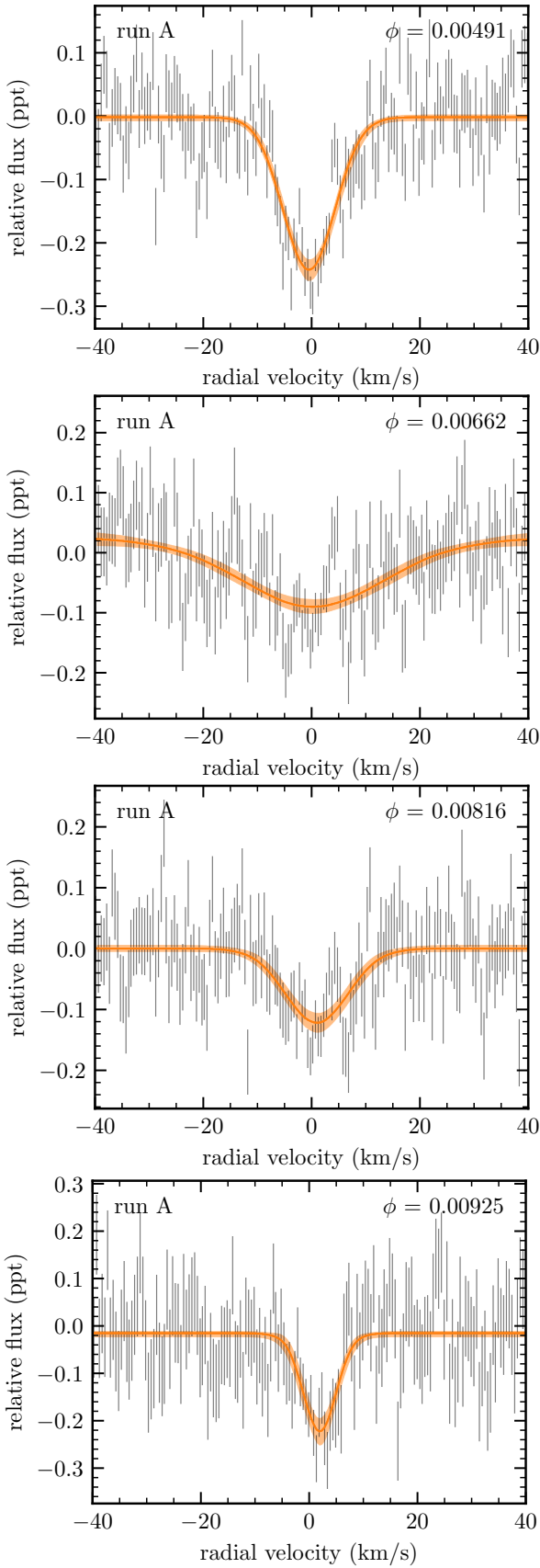


Figure C3. Gaussian fits to the 15 min binned residual line profiles from run A. The orange shading denotes the 1σ uncertainty of the model.

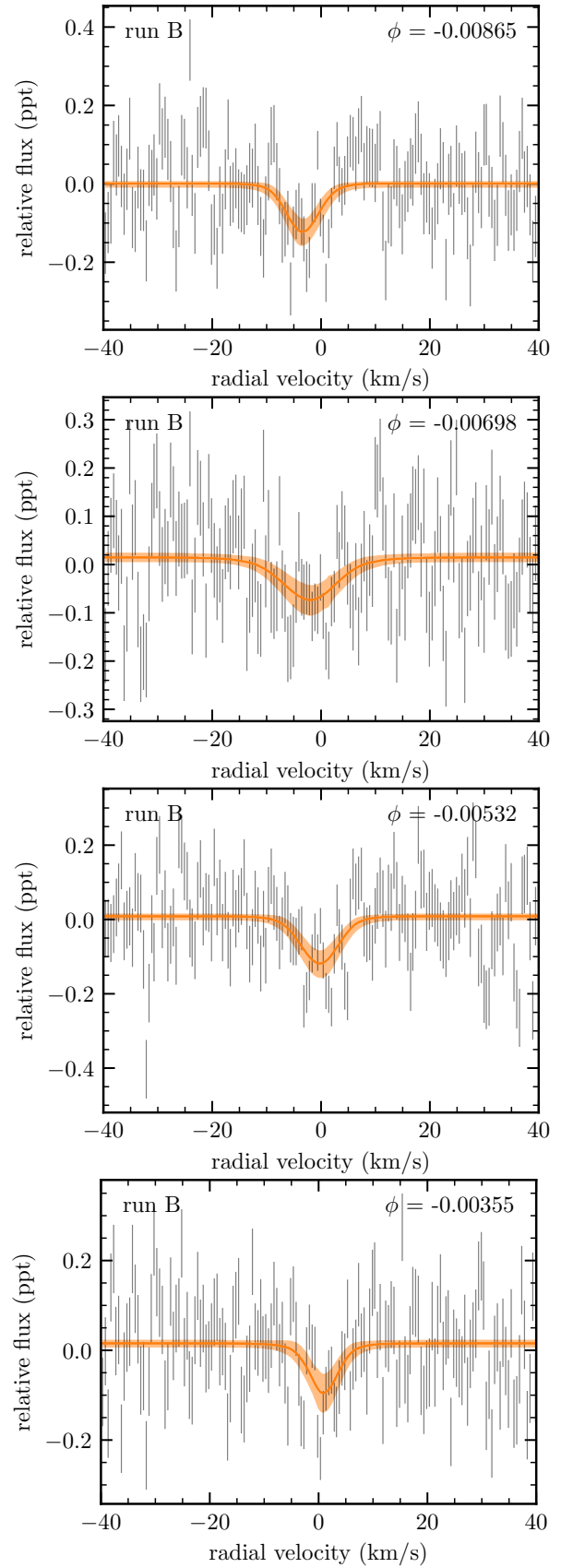


Figure C4. Gaussian fits to the 15 min binned residual line profiles from run B. The orange shading denotes the 1σ uncertainty of the model.

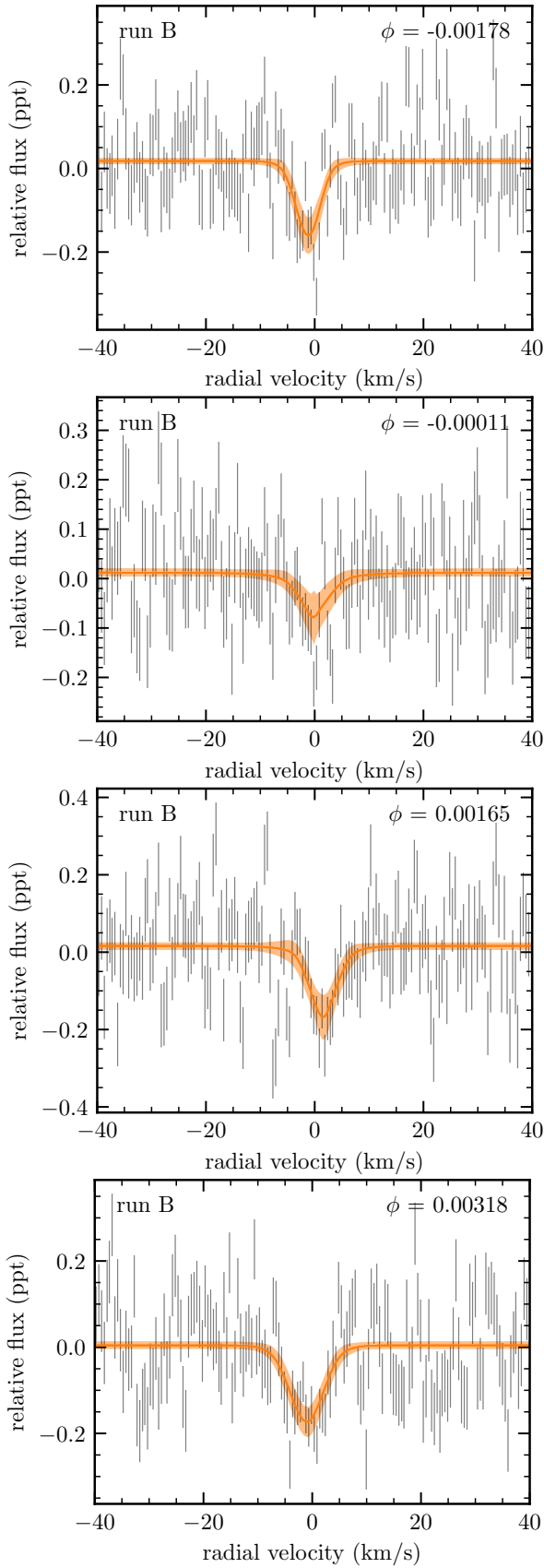


Figure C5. Gaussian fits to the 15 min binned residual line profiles from run B. The orange shading denotes the 1σ uncertainty of the model.

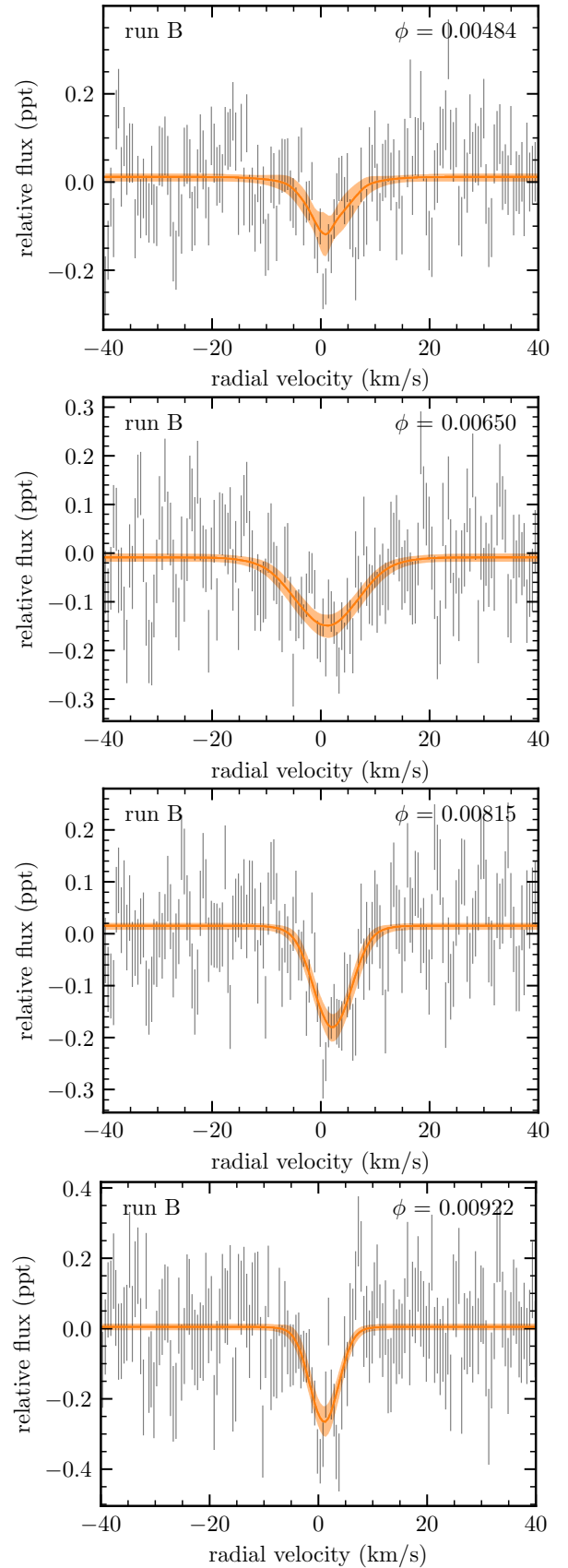


Figure C6. Gaussian fits to the 15 min binned residual line profiles from run B. The orange shading denotes the 1σ uncertainty of the model.

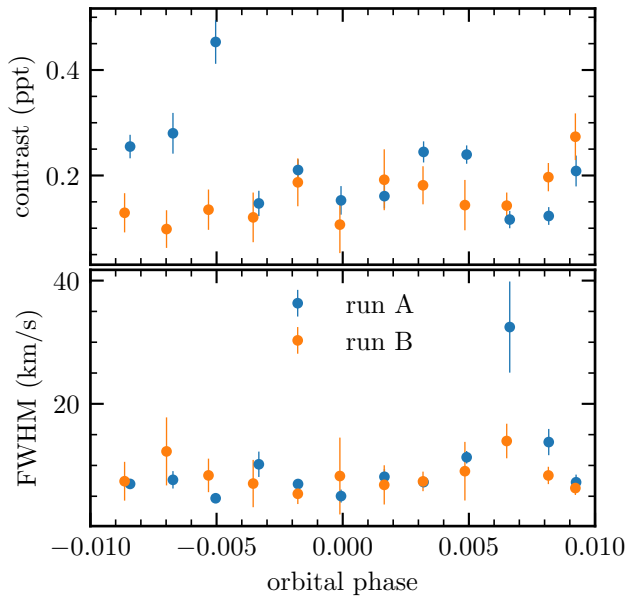


Figure C7. Comparison of the fitted local depth and width from the residual line profiles for run A and B.